Arctic freeboard and snow depth from near-coincident CryoSat-2 and ICESat-2 (CRYO2ICE) observations: A first examination during winter 2020–2021

Renée M. Fredensborg Hansen[1,2,3], Henriette Skourup[1], Eero Rinne[2], Knut V. Høyland[3], Jack C. Landy[4], Ioanna Merkouriadi[5], and René Forsberg[1]

[1]The Technical University of Denmark, DTU Space, Department of Geodesy and Earth Observation, Elektrovej Building 327, 2800 Kgs. Lyngby, Denmark
[2]The University Centre in Svalbard (UNIS), Department of Arctic Geophysics, P.O. Box 156, 9171 Longyearbyen, Norway
[3]Norwegian University of Science and Technology (NTNU), Department of Civil and Environmental Engineering, P.O. Box 8900 Torgarden, 7491 Trondheim, Norway
[5]Finnish Meteorological Institute, Earth Observation Research, P.O. Box 503, 00101 Helsinki, Finland
[4]UiT The Arctic University of Norway, Department of Physics and Technology, PO Box 6050 Langnes, 9037 Tromsø, Norway

Key Points:

- CRYO2ICE (C2I) snow depth at ∼7-25 km segments within CRISTAL requirements of uncertainty less than 0.05 m (precision used as proxy)
- Along-track snow depth is compared with basin-scale estimates, where C2I range lower for Canadian and Atlantic Arctic with similar spread
- Near-coincident dual-frequency snow depth is compared with in situ data from acoustic and thermistor-string buoys

Corresponding author: Renée Mie Fredensborg Hansen, `rmfha@space.dtu.dk`

Abstract

In the summer of 2020, ESA changed the orbit of CryoSat-2 to align periodically with NASA's ICESat-2 mission, a campaign known as CRYO2ICE, which allows for near-coincident CryoSat-2 and ICESat-2 observations in space and time over the Arctic. This study investigates the CRYO2ICE radar and laser freeboards acquired by CryoSat-2 and ICESat-2, respectively, during the full winter season of 2020–2021, and derives snow depths from their differences. As expected, the ICESat-2 signal is backscattered at a surface above the elevation of the CryoSat-2 signal. CRYO2ICE snow depths are thinner than the daily model- or passive-microwave-based snow depth composites used for comparison, where differences are most pronounced in the Atlantic and Pacific Arctic. These observations show the exciting potential for along-track dual-frequency observations of snow depth from the future Copernicus mission CRISTAL; but also highlight uncertainties in radar penetration and the length scales of snow topography that still require further research.

Plain Language Summary

Estimations of snow depth on sea ice are currently either outdated or limited in resolution, thus a need to derive high-resolution snow depth on sea ice is crucial. Former studies have computed snow depth on sea ice using the difference in penetration between radar (Ku-band) and laser (or Ka-band radar) altimeters from different satellite missions, assuming the Ku-band radar and laser/Ka-band are reflected at the bottom and top of the snow pack, respectively. However, those studies have resulted in monthly composites of snow depth due to a limited overlap of individual tracks between the satellite missions. Since the CRYO2ICE (CryoSat-2/ICESat-2 Resonance) campaign was initiated in July 2020, we have for the first time the possibility of investigating near-coincident observations of radar and laser altimeters. These results are important to initiate relevant discussions on snow depth retrieval in preparation of the future dual-frequency altimeter mission, CRISTAL (Copernicus Polar Ice and Snow Topography Altimeter), expected to launch in 2027.

1 Introduction

In July 2020, the European Space Agency (ESA) changed the orbit of CryoSat-2 (CS2) to periodically align with the National Aeronautics and Space Administration's (NASA's) Ice, Cloud and land Elevation Satellite-2 (ICESat-2, hereafter noted as IS2), a campaign named CRYO2ICE (CS2/IS2 Resonance Campaign, `https://earth.esa.int/eogateway/missions/cryosat/cryo2ice`, last access: 02 March 2022). This campaign increased CS2's orbital altitude by approximately 900 metres, and allowed for CS2 and IS2 to pass over near-coincident polar areas, targeting the Arctic until June 2022 when the subsequent CRYO2ICE Antarctic campaign was initiated. With the CRYO2ICE (C2I) campaign, CS2 and IS2 now pass approximately the same location at approximately the same time every 19/20 orbits (roughly every 31 hours, with a time difference between acquisitions of about 3 hours), allowing for near-coincident double-frequency observations over land and sea ice. The C2I campaign is the first of its kind and will advance our understanding of how different snow and sea ice properties may impact the signals received by satellite radar and laser altimeters. Furthermore, it will enable the investigation of known challenges comparing spaceborne altimetry measurements acquired at different frequencies and with different spatial resolutions.

An important parameter governing the growth and melt of sea ice is snow, due to its insulating and reflective properties. The depth of snow on sea ice vary on short spatial and temporal scales depending on weather patterns and surface conditions (Moon et al., 2019; Liston et al., 2018). Snow depth on sea ice has been obtained from spaceborne sensors using passive microwave observations (Markus & Cavalieri, 1998). However, these observations have relatively coarse resolution (12.5 km or more) and have been primarily obtained over first-year ice (FYI) (Markus & Cavalieri, 1998), limited to the spring for pan-Arctic coverage due to calibration with airborne observations (Zhou et al., 2021; Rostosky et al., 2018), or have simply not been provided as publicly operational, daily products. Snow depth on sea ice can also be estimated utilising the difference in penetration between spaceborne altimeters at different frequencies (e.g., Garnier et al., 2021; Kwok et al., 2020; Lawrence et al., 2018; Guerreiro et al., 2016). Monthly gridded estimates have been published using either laser and Ku-band (LaKu) altimeter observations (Kwok et al., 2020; Kacimi & Kwok, 2020, 2022) or Ka- and Ku-band (KaKu) altimeter observations (Lawrence et al., 2018; Guerreiro et al., 2016; Garnier et al., 2021) at both hemispheres, assuming that laser/Ka-band signals backscatter at or close to the air-snow interface and that the Ku-band signals fully penetrate the snow pack. However, recent studies suggest that this is not necessarily the case for all of the Arctic sea ice pack (King et al., 2018; Stroeve et al., 2022; Nab et al., 2023). Furthermore, the roughness within the footprint of the satellite at the scale of sea ice features (like ridges or leads) or small-scale roughness at the scale of the signal wavelength will likely also play a role in the derived variables (Landy et al., 2020). These techniques generally observe Arctic snow depths of about 0.10–0.15 m at the beginning of the winter season to about 0.20–0.25 m by the end of the winter. However, the methods typically filter or average the altimeter height differences over long intervals. Thus they do not resolve the local space-time variability of the snow depth nor the covariability between altimeter signals.

With the upcoming launch of ESA's CRISTAL (Copernicus Polar Ice and Snow Topography Altimeter) expected in 2027, it is important to investigate the potential of snow depth retrieval along the satellite orbit, as CRISTAL will carry a dual-frequency (KaKu) altimeter capable of retrieving snow depth variability along track. One of the mission requirements of CRISTAL is to provide sea ice freeboard (height of sea ice above local sea level) with an accuracy of 0.03 m along orbit segments of less than or equal to 25 km, and deliver sea ice thickness measurements with a vertical uncertainty of less than 0.15 m along the same orbit segments (Kern et al., 2020). To achieve this, snow depths need to be obtained along the same orbit segments with an uncertainty of less than or equal to 0.05 m (Kern et al., 2020). This calls for an urgent investigation of altimeter-derived snow depth along orbit-segments of 25 km or less, which the C2I campaign provides the first-ever opportunity to investigate. The difference between radar and laser freeboards, assuming that the Ku-band radar (CS2) signal penetrates through the entire snow pack to the snow-ice interface (Kacimi & Kwok, 2020) and that the laser (IS2) is backscattered from the air-snow interface, can be used to derive snow depth along the C2I orbits with high spatial and temporal resolution. Detailed observations like this can be used to examine the assumption of full CS2 signal penetration when compared with reference observations, which is crucial since uncertainties on the snow load and signal penetration constitute the largest sources of error in sea ice thickness estimates derived from altimetry (Landy et al., 2020). Providing such high-resolution observations of snow depths will likely reduce the uncertainty in sea ice thickness observations from altimeters, since they currently rely on an estimate of snow mass loading to compute sea ice thickness which is often provided by a climatology (Warren et al., 1999), a fusion of climatology/passive microwave observations (Hendricks & Ricker, 2020) or reanalysis-based reconstructions (Stroeve et al., 2020). Furthermore, such snow depth maps can also be used to assimilate into models and to improve the simulation of heat fluxes through the ice and albedo changes in spring (Webster et al., 2018), while providing new information about precipitation events and re-distribution of snow on sea ice (Liston et al., 2021). By using observations from this new C2I constellation, we will retrieve highly valuable and timely information to the sea ice community, prior to the launch of CRISTAL. However, there are limitations and challenges of comparing data from different sensors with different resolution and assumptions applied, some of which we will address in this study.

The aim of this study is to make a first examination of the feasibility of obtaining snow depth observations over sea ice using the difference between laser and radar freeboards from near-coincident observations. The study will discuss steps for making observations of different resolution comparable over sea ice and present first results of snow depth from C2I observations. These observations will be compared with auxiliary snow depth data derived from passive-microwave observations and reanalysis-based models. Furthermore, aspects that may impact the derived freeboard observations will be discussed in relation to the derived snow depth estimates. This study will provide insight into the comparison of altimeter data over sea ice with different footprint scales, for capacity building before the launch of CRISTAL.

2 Data and methods

For this study, we investigate C2I observations from the first winter season (November 2020 through April 2021). By investigating a full winter season we expect several processes to have occurred within the snow- and ice pack (e.g., snow grain metamorphism, flooding, refreezing, differences in snow depth due to accumulation of snow throughout the season, deformation of ice resulting in increased surface roughness, possibly melting, freeze-up, measurements of thinner ice or thicker ice), all affecting the snow pack on the ice and potentially the mechanisms by which the altimeter radar and laser signals interact with the snow.

2.1 IS2 data

IS2 is a photon-counting laser altimeter which transmits laser pulses split into a six-beam configuration of three beam pairs (each having a strong and weak beam), where beam numbers 1, 3, and 5 identify the strong beams, and 2, 4, and 6 the weak beams (Neumann et al., 2019). With a 10 kHz pulse-repetition-frequency, it leads to a 0.7 m along-track separation and allows for an unprecedented dense surface-sampling at footprints of about 11 m at nominal altitude (Magruder et al., 2020). From these photons, surface segments are derived by aggregating 150 photons, and based on a radiometric classification, segments from leads and floes are identified and produced in the ATL07 product (Sea Ice Heights). Along-track freeboards are calculated in the ATL10 product based on a reference sea surface derived from the available lead/sea surface segment heights. A single reference sea surface estimate is produced for consecutive 10 km along-track sections that include at least one sea surface sample, for each beam independently. Freeboard segments are then derived by differencing the sea ice segment heights from the local 10 km reference sea surface height. Negative freeboards are set to zero (Kwok et al., 2020; Petty et al., 2021). IS2 observations are constricted when in the presence of clouds, which for the photon product (ATL03) is reflected as either noisy photons (thin cloud cover or fog) or photons being reflected at the top of the cloud cover (Fredensborg Hansen et al., 2021). These are removed during processing which results in gaps along the track (e.g., Figure S2). ATL07 recently refined the surface finding procedure (the identification of leads for sea surface height segments), where surface classifications such as dark leads have been removed (keeping only specular returns as leads) which has improved the performance. When selecting the IS2 data to include in this analysis, we must consider the beams to include: both when it comes to beam pairs and weak/strong beams. Bagnardi et al. (2021) recently showed that for sea surface height anomalies, the strong beam of one beam pair was less correlated with the other strong beams, suggesting an elevation bias between the beams. However, we expect this to have little impact on freeboard observations, as they are relative observations within the same beam. A recent study (Ricker et al., 2023) also suggested that weak beams, with $\sim 1/4$ of the photon rate compared to strong beams, can provide useful information along the track and should be considered even if this is not what the operational monthly freeboard product (ATL20) currently does (Kwok et al., 2022). Based on these findings and due to the limited coverage of C2I observations, we shall include all six beams when binning the data to comparable resolutions (Section 2.5).

2.2 CS2 data

CS2 data has a larger footprint (~300 m x 1600 m in SAR mode and samples at a rate of 20 Hz, about every 300 m) than IS2, thus it will be used as the reference resolution for the C2I observation to ensure the highest spatial resolution possible when comparing sensors. To examine the sensitivity of the freeboard and snow depth to different re-tracker (a processing estimation approach used to determine the range to the ground target) and/or processing methods, we have included three different products: two using empirical re-trackers, and one using a physical re-tracker.

- **Baseline-D Ice radar freeboard (ESA-D)**: We use data acquired by the SIRAL Ku-band interferometric synthetic aperture radar (SAR) altimeter in SAR mode, the primary mode over sea ice, mounted on CS2. We make use of both Level 1b (L1b) and Level 2 (L2) Ice products processed at the Baseline-D version (Meloni et al., 2020), which is publicly available from ESA's FTP server (`ftp://science-pds.cryosat.esa.int/`, last access: 02 March 2022). At the time of writing, the updated baseline (Baseline-E) for CS2 had not been reprocessed to include the winter 2020–2021, thus we use the Baseline-D observations. We extract the radar freeboard, which has been derived using combined waveform re-trackers: (a) for diffuse waveforms, expected to originate from ice floes, a 70% threshold-of-first-peak re-tracker developed by the Centre for Polar Observation and Modelling, and (b) for specular echoes, expected to originate from leads, a peak-finder based on the model-fitting method described in Giles et al. (2007). CS2 ESA-D data have been pre-processed to remove erroneous points using the error flags available in the L2 product following the procedure described in Text S1.
- **Lognormal Altimeter Re-tracker Model (LARM) radar freeboard**: Landy et al. (2020) presented a physical a re-tracker which varies the percentage threshold that is being re-tracked according to the large-scale roughness of the sea ice, based on model simulations of the radar altimeter echo assuming a log-normal distribution of the surface roughness (Landy et al., 2019). The same re-tracker is also automatically applied to leads, which have negligible roughness and therefore a re-tracking threshold >98%.
- **Climate Change Initiative+ (CCI+) radar freeboard**: Another commonly used CS2 product is the CCI+ Climate Record Data Product (CRDP), which also employs the empirical first-threshold-of-peak re-tracker, however with a percentage threshold of 50% for both sea ice floes and leads.

It may be the case that for some ESA-D observations there are no CCI+ or LARM observations available, or vice versa, due to different filtration schemes applied by the providers. However, when comparing statistically, we shall only compare observations where there is coverage by all three re-trackers unless otherwise noted. The pre-processing steps and steps to identify corresponding observations between different datasets are discussed in Text S1.

2.3 Independent data

A comparison between the derived C2I snow depth and independent snow depth estimates is necessary to evaluate the performance of the algorithm. Due to limited coverage by C2I and lack of dedicated reference campaign observations, we have limited in situ observations to compare with. Instead, we will primarily compare C2I-derived snow depth with snow depth estimates computed from passive microwave observations over first year ice and reanalysis-based numerical snow evolution schemes for all sea ice types. This comparison is not meant as a validation, since we cannot be sure that any of these products represent the truth. However, the comparison provides a means of evaluating the snow depths derived from altimetry against the state-of-the-art snow products currently used for scientific applications including estimating sea ice thickness.

2.3.1 Basin-scale estimates

Of available Arctic snow depth products at daily resolution, we have identified two contrasting ones: a passive-microwave derived snow depth product and a reanalysis-based snow model, both provided in gridded formats. For each available C2I snow depth observation, the nearest gridded point from the basin-scale estimates are extracted and used for comparison. The distance between points is calculated based on the haversine formula for a spherical Earth.

- **Advanced Microwave Scanning Radiometer (AMSR2)**: We make use of the daily snow depth product, computed following the methodology of Markus and Cavalieri (1998), which excludes the Arctic perennial ice regions due to microwave volume scattering making retrieval of snow depth on multi-year ice (MYI) ambiguous. The snow depth retrieval methodology of AMSR2 is applicable only to dry snow (Meier et al., 2018). We further extract sea ice concentration parameter computed using the method described by Markus and Cavalieri (2000, 2009). Both snow depth and sea ice concentration are provided on a swath-level basis and afterwards averaged out daily to a 12.5 km polar stereographic grid.
- **SnowModel-LG (SMLG)**: SnowModel-LG (SMLG) is a snow evolution modelling system that produces daily snow depth and density distributions over Arctic sea ice from August 1, 1980, and onward. SMLG resolves physical snow processes such as sublimation from static surfaces and blowing snow, snow melt, snow density evolution, snow temperature profiles, energy and mass transfers within the snow pack, and superimposed ice (Liston et al., 2020). SMLG was recently coupled with a 1D thermodynamic sea ice model (HIGHTSI; Launiainen & Cheng, 1998), to account for snow loss in snow-ice formation, i.e., ice that forms at the sea ice surface as a result of flooding at the snow/ice interface due to negative freeboard conditions (e.g., Leppäranta, 1983). Snow-ice formation results in the reduction of snow depth over sea ice, with part of the bottom snow layers being incorporated into the sea ice (Merkouriadi et al., 2020). In the updated product (SMLG-HS) snow depth and density are modified accordingly when conditions favour snow-ice formation (Merkouriadi & Liston, 2022).
- **(Warren et al., 1999) (W99) and modified W99 (mW99)**: W99 presents a pan-Arctic monthly (October–April) climatology of snow depth estimates derived from reference observations carried out during the 1950-1990s (Warren et al., 1999). Kurtz and Farrell (2011) showed, through a comparison with airborne observations, that W99 overestimates snow depth estimates of FYI by about a factor of 0.5. Thus, it is common practice for altimetry studies using W99 to apply this correction factor. We shall use these available climatologies primarily to compare accumulation patterns as they are in situ-based. W99 is available through the CS2 L2 product, and mW99 was provided as part of a gridded LARM product (available via this study's data package).

2.3.2 In situ reference measurements

There were no successful Arctic airborne campaigns dedicated to the C2I campaign during the period of the study (primarily due to COVID-19), and due to the sparse coverage of C2I orbits, the quantity of available reference measurements are limited (see Text S2 for discussion on available reference observations). However, both seasonal ice mass balance (SIMBAs) and acoustic snow depth buoys were deployed during the final leg of the MOSAiC (Multidisciplinary drifting Observatory for the Study of Arctic Climate) expedition, and we shall utilise observations from these for a comparison. The acoustic buoys deployed by the Alfred Wegener Institute (AWI) consist of four ultrasonic sensors, which each measures its distance from the snow's surface. It is therefore not the actual snow depth that the sensors measure, but instead the accumulation and ablation of the snow surface relative to the initial snow depth, that is converted to snow depth (Nicolaus et al., 2021). In total, we identified five acoustic buoys (deployment reports available on Grosfeld et al. (2016, last access: 2023/05/12): 2020S98, 2020S105, 2020S106, 2020S107, and 2020S108, but only three of the buoys (2020S108, 2020S106, and 2020S105) had coincident snow depth measurements with our C2I study period. In addition, several SIMBA buoys were deployed. While not currently published, snow depth estimates from two of the buoys were provided for this study by the contact persons listed in Grosfeld et al. (2016). FMI0607 (also noted as 2020T84) was deployed on level first-year sea ice with initial thickness of 1.14 m and snow depth of 0.03 m. PRIC0906 (or 2020T85) was deployed on a ridge where sea ice thickness was >4 m with initial snow depth of 0.05 m. Both buoys carried a thermistor-string frozen into the sea ice. From the changes in the vertical temperature profile, the location of air-snow, snow-ice and ice-water interfaces can be estimated, providing information of the snow depth and ice thickness (Jackson et al., 2013; Liao et al., 2019). When comparing with reference observations, the buoy observations are first post-processed to daily snow depth estimates at the average daily location. We identify comparable C2I points assuming they are within +/- 50 km and 2 days of the buoy locations and acquisition time similar to Ricker et al. (2015).

2.4 Identification of relevant C2I data

Utilising the publicly available C2I tool (`www.C2I.org`, last access: 02 March 2022; now updated to `www.cs2eo.org`) developed by EarthWave (Alford et al., 2021), we identified relevant C2I orbits for the period of November 2020 to April 2021. We retrieved monthly C2I tracks provided the CS2 and IS2 orbits were within a 10 km separation distance, had less than 4 hours between the respective acquisition times and that the intersection time of the orbits were more than 1 minute. Using these criteria, the tool identified 530 C2I segments for the winter season of 2020–2021. However, the identified segments in the C2I tool are not necessarily equivalent with the full-length of a C2I orbit i.e., C2I-identified-segments are not equivalent with a full C2I track but rather sub-parts of the same track. The segments can be limited due to e.g., data unavailability of IS2 caused by the presence of clouds or limitations of the retrieval methodology, and as such one full C2I track may have several identified segments. Therefore, a manual selection of the extracted CS2 and IS2 tracks was conducted from which 389 C2I tracks (Table S1) were identified for further analysis. Application of the full pre-processing and data binning methodology (Section 2.5) resulted in a total of 358 C2I tracks used for this study, relatively evenly spaced in time and geography, over the winter season under investigation (Figure S2).

2.5 Data binning of C2I data

The aim is to obtain the highest spatial resolution of the estimated snow depth as possible i.e., close to the sampling interval of CS2, however the real challenge is ensuring that the CS2 and IS2 observations are statistically comparable after binning. The distance of the IS2 sample from the closest beam to the nadir point of CS2 is, on average, 2391.79 +/- 356.51 m (Figure S3, using a maximum radius of 3500 to include all six beams). Thus, we are likely to require a radius for binning the observations that is larger than the radius of the CS2 pulse-limited footprint ($\sim$850 m, as was used in Bagnardi et al. (2021)), with observations from the two sensors rarely coinciding exactly. Since IS2 points closest to the CS2 observation should be more representative of the surface observed by CS2, we give a higher priority to these points. Therefore, the downsampled IS2 freeboard observations are derived with linear inverse distancing weights applied. However, it is still important to consider how large a search radius, centered at each CS2 nadir point, to be used when binning IS2 to the same location as CS2. The choice of search radius is a compromise between the spatial coverage (along-track number and density of snow observations along C2I track) and representation of the surface. The analysis presented in Figure S4 and Text S3 shows the variance of the freeboard differences between CS2 and IS2 as a function of the along-track binning radius. It is evident from Figure S4 that the variance is higher for a search radius equalling the CS2 pulse-limited footprint than for higher search radii; however, the variance decreases to a saturation point around 2000 m. We conclude that a search radius of 3500 m provides comparable results to the case where we use a lower search radii, but increases the number of observations. It is also worth mentioning that the radar observations are inherently noisy, and as such, the freeboard observations will also be noisy. Some of the processing steps may have included smoothing e.g., the sea surface height anomalies interpolated to ice floe locations might have been smoothed, but nonetheless at the nominal 20 Hz CS2 sampling rate the freeboards will be noisy. This will become less important once we consider averages over orbit-segments of 25 km i.e., the CRISTAL requirement, but will be kept here to discuss the differences between what IS2 and CS2 is observing. To make the IS2 and CS2 further comparable, we smooth the CS2 freeboards with a 3500 m radius as well (∼7 km moving average window), limiting the impact of speckle noise in the process. When generating orbit-based segments of 25 km, we have separated the along-track distance into segments of 25 km and appointed the observations to the nearest segment point using the haversine formula.

2.6 Snow depth from differences in laser and radar altimetry

Following the methodology of Kwok et al. (2020), we calculate the snow depth by differencing laser and radar freeboards. Assuming a simple-layer geometry of sea ice floes, one can express snow depth (h_{fs}) as the difference between the total freeboard (h_f), as measured by IS2, and the sea ice freeboard (h_{fi}):

$$h_{fs} = h_f^{IS2} - h_{fi}. \tag{1}$$

The sea ice freeboard (h_{fi}) can be related to the radar freeboard measured by CS2 (h_{fi}^{CS2}) following:

$$h_{fi} = h_{fi}^{CS2} + h_{fs}(\eta_s - 1). \tag{2}$$

Here, η_s is the refractive index at Ku-band, $\eta_s = c/c_s \cdot (\rho_s) = (1+0.51\rho_s)^{1.5}$ (Ulaby et al., 1986), and c is the speed of light in free space. The second term in Equation 2 accounts for the reduced propagation speed of the radar wave (c_s) as it travels through the snow pack with a bulk density ρ_s. It is assumed, that at temperatures below freezing, at the wavelengths of IS2 and CS2, that the laser and radar returns can be assumed to be from the air-snow and the snow-ice interfaces, respectively, resulting in observations of total and sea ice freeboards. The validity of this assumption has been discussed in several studies (Nandan et al., 2017; Tonboe et al., 2021; King et al., 2018), and implications thereof are discussed in Section 3. Through combination of equation 1 and 2 and solving for h_{fs}, snow depth is given by:

$$h_{fs} = \frac{\left(h_f^{IS2} - h_{fi}^{CS2}\right)}{\eta_s} \tag{3}$$

Now, snow depth (h_{fs}) is related to the differences between the IS2 and CS2 freeboard (the observables) with one free parameter, η_s, which is dependent on the bulk snow density. For this study, we shall keep the bulk density of snow constant at 300 kg·m^{-3}, producing $\eta_s = 1.24$, and discuss the impact of this assumption further in Section 3. The equations defined here also follow the definitions of Garnier et al. (2021).

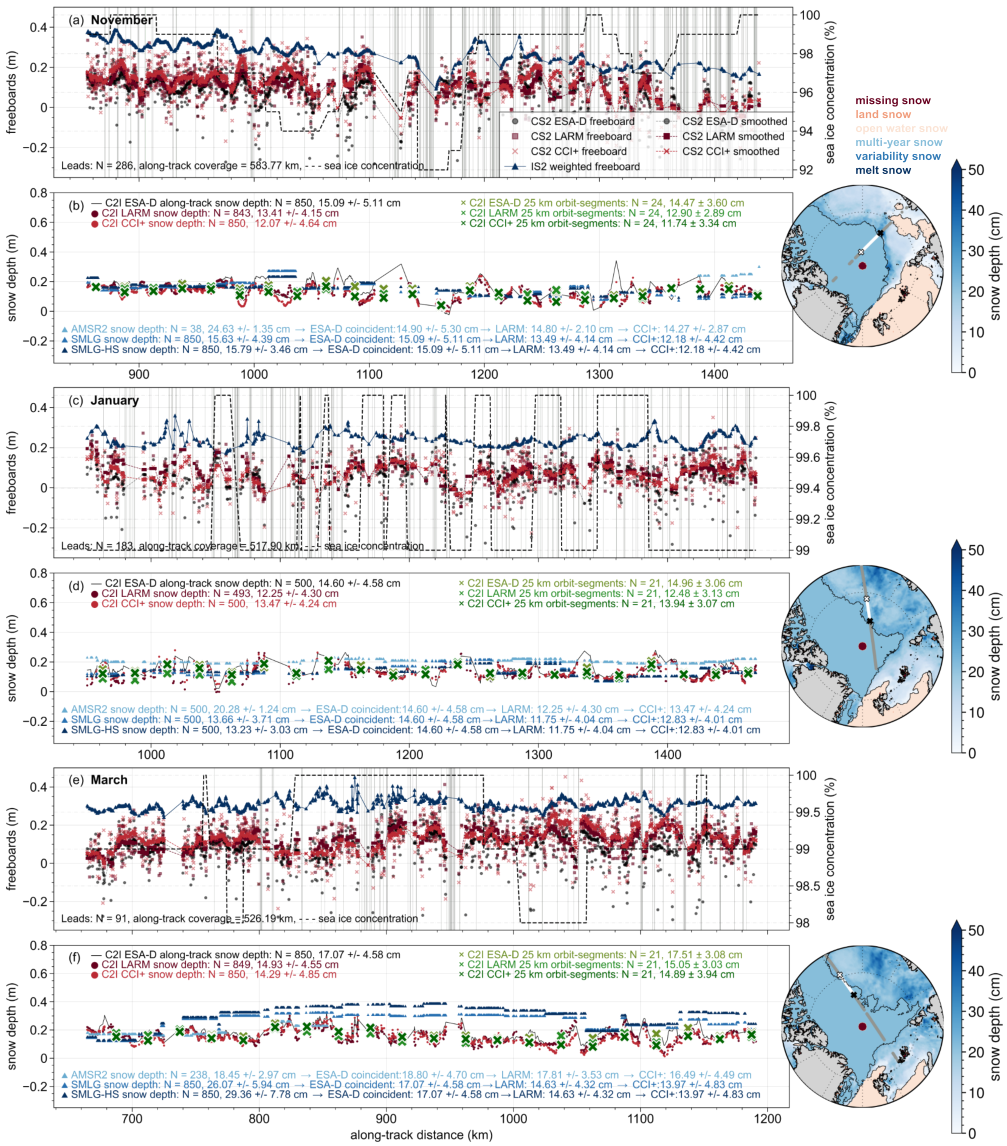

Figure 1. Subset of CRYO2ICE (C2I) track with (a) CryoSat-2 (CS2) Baseline-D (ESA-D), Lognormal Re-tracker Altimeter Model (LARM) and Climate Change Initiative (CCI+) radar freeboard, ICESat-2 (IS2) weighted laser freeboard and associated AMSR2 sea ice concentration for 10 November 2020. CS2 ESA-D identified leads are shown in vertical grey lines, number of leads in the subset is denoted on the subplot along with the along-track coverage of the subset; (b) C2I along-track snow depth using different re-trackers and associated snow depth from AMSR2 and SMLG/SMLG-HS for 10 November 2020. C2I snow depths at 25 km orbit segments (one value pr. segment) are provided as well. The pan-Arctic map showing AMSR2 snow depth estimates and classifications (open water, multi-year ice etc., presented by the legend above the first map) also shows the location of the track and subset; grey denote the entirety of the track, white is the subset of the C2I track, white cross denotes the beginning and black cross the end of the subset; (c-d) same as (a-b) for C2I track on 30 January 2021; (e-f) same as (a-b) for C2I track on 17 March 2021.

3 Results and discussion

3.1 Freeboards and associated snow depths along-track

The freeboards of CS2 and IS2 binned to a similar resolution (C2I) are shown for one pair of tracks in November, January, and March in Figure 1a, c and e, respectively. The tracks are ∼500 km long. Here, it generally shows that IS2 has higher freeboards than CS2, as expected based on the assumption that IS2 pulses are reflected at the snow-air interface (typically the first surface encountered). However, it can be seen several times how CS2 exceeds the freeboards observed by IS2. This could be due to: (a) the binning methodology, where more of the used IS2 points originate from level/thinner ice whereas the paired CS2 point is sensitive to thicker ice or an area of rougher surface topography; (b) noise/speckle in the CS2 data; or (c) noise in the IS2 data. Significantly more leads are observed in the track from November than in January or March. This is expected, due to the thinner and less dense ice cover in November compared to a consolidated ice cover at the end of the winter in March. However, the presence of leads can also impact the derived freeboard. In areas where there is more open water and leads, the waveforms are more likely to experience off-nadir reflections and snagging (Armitage & Davidson, 2014), which will bias the CS2 radar freeboard high. However, in most cases, these snagged waveforms will be removed by the quality flag in the pre-processing or flagged as 'ambiguous' in the waveform classification routine and discarded. Furthermore, having a limited number of lead observations will impact the interpolated instantaneous sea surface height anomalies observed from the leads, and as a consequence impact the derived freeboard. As an example, we see a drop in sea ice concentration in November around 1150 km along-track, which coincides with raw CS2 freeboards being higher than IS2 total freeboards. This will result in negative snow depths, but is likely caused by the presence of open water in the footprint of CS2 which impacts the waveforms, and hence the re-tracked surface elevation.

From these freeboards, we can derive snow depths following Equation (1), which are shown in Figure 1b, d, and f. The C2I CS2 freeboards at raw sampling rate show higher along-track variability which will result in higher snow depth variability when compared to the SMLG and AMSR2 observations available at 12.5–25 km resolution. Through the comparisons of observations from three different re-trackers, we investigate differences in snow depth depending on the selection of re-tracker. The LARM product overall has the fewest points for comparison, which might suggest that the re-tracker is either more sensitive to complex waveforms or has stricter requirements in the selection of non-contaminated waveforms. It is noteworthy that the re-trackers are most consistent over the track from January covering only FYI, which may suggest the freeboard is most sensitive to the re-tracking step over MYI. This is likely due to the increased surface roughness occurring over MYI as well as an increased complexity of the MYI snow pack impacting the radar scattering surface to potentially occur within the snow pack, particularly pronounced by the end of the winter season (March track). To limit the impact of speckle noise, we smooth the CS2 freeboards using a search radius of 3500 km (∼7 km window) similar to the binning of IS2 freeboards. Applying a smoothing filter decreases the variability to be within the range of the basin-scale estimates, and for these examples, shows the potential of deriving snow depth estimates with a precision requirement (here, shown by standard deviation across ∼500 km tracks) that would decrease the snow depth uncertainty and align with the CRISTAL requirements. It is important to note, that CRISTAL mission requirements presented in Kern et al. (2020) only note uncertainty requirements or not precision requirements. Since the operational products of CS2 and IS2 do not provide uncertainty estimates, we cannot derive an uncertainty estimate for this snow depth product, and shall use precision as a proxy of uncertainty knowing that it will also depend on the uncertainty of the freeboard estimate.

While the comparison data of basin-scale estimates are from gridded products and of coarser resolution with less variability, it still provides an interesting comparison. For the track in January, we have a significant number of comparable observations, and on average along the track AMSR2 appears to observe consistently thicker snow than C2I and SMLG, which may be due CryoSat-2 not penetrating through to the snow-ice interface or AMSR2 overestimating the snow depth. In comparison, the track of March has some points to compare (N = 238) and here, the AMSR2 observations are close to the C2I observations. In the comparison with SMLG/SMLG-HS, observations along the entire C2I track are provided and thus, a more comprehensive evaluation can be done. Here, higher similarity is observed between the tracks of November and January when comparing with average observations (0.02-0.04 m of difference) and along the track. SMLG/SMLG-HS also observes more variability than AMSR2 snow depths, and has a more consistent variability to the C2I observations. Large differences are observed in the track of March, with SMLG/SMLG-HS seeing 0.10-0.15 m thicker snow than the C2I observations. In SMLG this identifies new snow accumulation that has occurred during the season, and is thicker than C2I which has a snow depth similar to January albeit for a different location. This highlights the challenge of CS2 potentially not being able to fully penetrate the snow pack over MYI. As an example, SMLG consistently shows high snow depth with little variability between 800-1000 km along-track in March, whereas C2I shows high variability with overall lower snow depths for the same location (Figure 1f).

3.2 Comparison between C2I snow depths observations and other basin-scale estimates with in situ reference measurements

In situ observations of snow depth on sea ice are scarce, but buoys (acoustic and thermistorstring) were identified for the period of 2020-2021 (Section 2.3.2). Here, we observe for the acoustic buoys (Figure 2a-d) significant accumulation of snow that is not reflected in the C2I or model estimates. Overall, the acoustic buoys show snow depth values up to 0.70 m, with averages of 0.30-0.45 m across the entire acquisition period. For coincident C2I points, the average buoy snow depth is 0.44 m where the C2I ranges between 0.12-0.16 m and SMLG/SMLG-HS estimates between 0.16-0.21 m. The periods of rapid increase in acoustic buoy snow depth, in November 2020 and January 2021, elevate the in situ snow depth well above the satellite and model estimates. The higher snow depths from these buoys are likely caused by snow accumulation around and on the sensors (see Figure S5 and Text S4), leading to an potential overestimation of the in situ recorded snow depth. Such rapid increases has been observed previously (Nicolaus et al., 2021); however, we cannot be sure these measurements are unrealistic on floe scales.

The SIMBA buoys (Figure 2e-h) show more comparable snow depth accumulation patterns to the satellite and model-based estimates. It is worth noting that PRIC0906 was deployed on a ridge, which will result in a different accumulation pattern than expected on level sea ice. Here, the top of ridges are likely to experience thinner snow depth due to wind re-distribution (Liston et al., 2018), with the wind/blown snow accumulating around the ridges in sheltered areas causing deformed ice to have thicker snow depths (Sturm et al., 2002). The statistics provided in Figure 2f includes both SIMBA buoys, but if we focus first on the buoy deployed on level ice (Text S5, Figure S6 and Table S2), the FMI0607 and the C2I and SMLG-HS snow depths have moderate positive correlations (0.46-0.58), but with C2I underestimating the in situ snow depth. Figure 2h shows a similar accumulation pattern for FMI0607 and the C2I snow depth estimates. For the PRIC0906 buoy deployed on a ridge, the in situ snow depth significantly underestimates SMLG (by +0.20 m after February) but is more consistent with the snow depths from C2I ($\sim$0.10-0.15 m). Overall, for the thermistor-string buoy deployed on level ice, the results are comparable and with decent correlations. We combined PRIC0906 and FMI0607 to reflect the different (deform and level) ice that can be observed within C2I resolutions (Figure S7, Table S3). Here, moderate correlations (0.32-0.48) where observed with small bias (ranging between 0.01-0.4 m) for C2I estimates and SMLG-HS. It is clear from these comparisons that making a firm conclusion on the accuracy of C2I or SMLG/SMLG-HS snow depths with a few in situ time series is challenging. Therefore, to fully examine the capabilities of C2I snow depth retrieval, it is necessary to compare with near-coincident reference observations distributed over time and space, preferably from airborne or ground-based campaigns with similar instruments. That will be the aim of future work, when the CRYO2ICE Antarctic under-flight, conducted on the 13th of December 2022 as part of the ESA Cryo2IceEx/NERC DEFIANT campaign, will be investigated.

3.3 Variations of coincident C2I snow depths across the winter season 2020–2021

We investigate a full winter season of observations to evaluate how well the C2I observations compare with dual-altimetry observations at pan-Arctic monthly scales. Here, we present the distributions of C2I snow depths at 25-km segments separated into three study regions (Figure 3, areas defined in Figure S2). Here we note from the pan-Arctic maps that thicker snow is present over the Canadian Arctic (CA) and thinner snow over the marginal seas (Pacific and Central Arctic (PA), and Atlantic Arctic (AT)). C2I snow depths in CA reach approximately 0.20 $\pm$ 0.065 m (one standard deviation) by the end of the accumulation season, whereas SMLG/SMLG-HS observes slightly thicker snow depths with wider distributions of approximately 0.23 $\pm$ 0.065 m. The largest discrepancies between the model and C2I observations occur in the AT and PA regions, where C2I observes lower snow depths with a narrower distribution. This is correlated with the storm tracks and precipitation events that act to enhance snow depth in the model, especially later in the accumulation season, that is not represented in the satellite observations (Zhou et al., 2021). The satellite observations generally observe thicker snow in CA which reduces gradually to thinner snow across the Atlantic and Pacific sectors (Kacimi & Kwok, 2020; Garnier et al., 2021; Guerreiro et al., 2016; Lawrence et al., 2018). It is worth noting that the acoustic snow buoys observed clear snow accumulation events in spring 2021, whereas spring accumulation was very low or absent in the SIMBA observations (Figure 2), which suggests that both the satellite observations could be missing information or the models may overestimate, but also how comparison with local-scale buoy estimates can prove challenging.

We also investigate bimonthly snow depth distributions of a full pan-Arctic coverage of gridded IS2/CS2 (LaKu) snow depths for the winter season 2020–2021 (Figure S8). Here, thinner snow depths are observed for PA in the beginning of the season compared to C2I with similar snow depths observed by the end of the season. There is higher variability for gridded snow depths in CA than observed by C2I. The differences in the shapes of the distributions can be related to the difference in data coverage between C2I and LaKu. For instance, the much thicker snow of CA (tail and bimodality of distribution) is not observed in C2I due to limited observations in the area directly north of Ellesmere Island and Greenland. The inconsistent and incomplete C2I data coverage across the Arctic also impacts the estimation of the seasonal snow accumulation rates (Figure S9-S11). Here, the accumulation rates are separated into zones of first-year and MYI (based on AMSR2 ice type classification). Over FYI the C2I snow depths accumulate by $\sim$0.09 m with similar magnitude and at a very similar rate to the SMLG estimates. However, the snow depths from W99 and AMSR2 are much thicker, by $\sim$0.12 and $\sim$0.08 m, respectively. We note, that recent studies have shown that snow depths from W99 should be multiplied by a factor of 0.5 over FYI for recent years (Kurtz & Farrell, 2011), thus we expect W99 to have thicker estimates. Over MYI, the C2I snow depths are similar to SMLG at the beginning of the season but $\sim$0.07 m thinner by April, and 0.15 m thinner than those from W99. The dense region of C2I observations close to the polar hole, as well as the entire CA area, are classified as MYI using AMSR2, where the snow depth accumulation rates show limited accumulation.

To investigate the seasonal accumulation in the Central Arctic in more detail, we have studied the average IS2 and CS2 freeboards individually (Figure S10). Here, we see that IS2 increases by only approximately 0.065 m across the season although, in com-

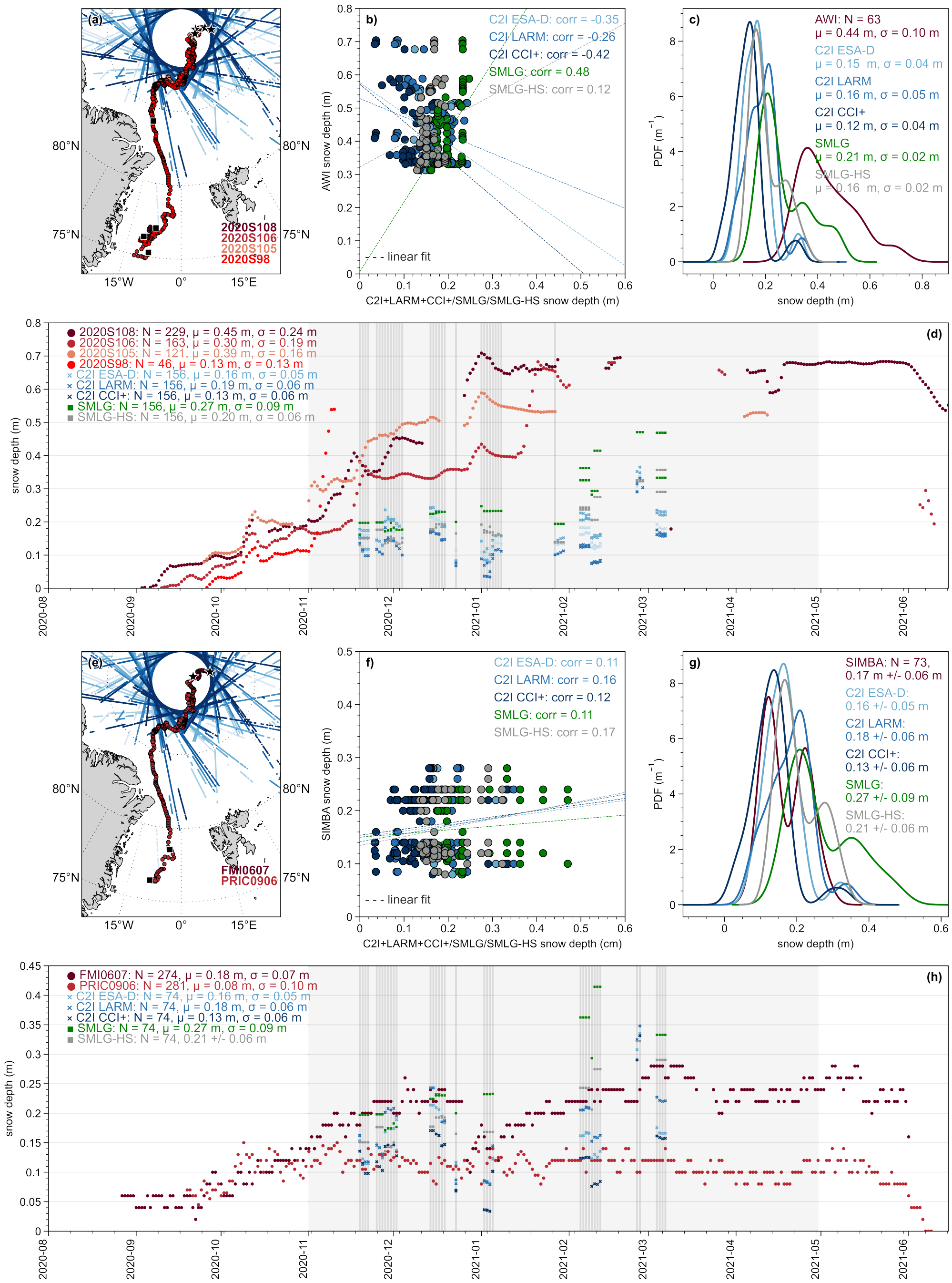

Figure 2. Comparison against Alfred Wegener Institute (AWI) and Seasonal Ice Mass Balance Array (SIMBA) snow depth buoys. (a) location of buoys overlaid C2I 2020-2021 tracks (Nov-Apr). (b) comparison between coincident buoy and C2I/SMLG/SMLG-HS snow depths (within +/- 50 km and 2 days). (c) distribution of coincident snow depth observations. (d) full time-series of snow depths from coincident buoy/C2I/SMLG/SMLG-HS observations. Grey lines indicates coincident observations. There were no overlap between the buoys and AMSR2 observations. (e-h) same as (a-d) for SIMBA buoys.

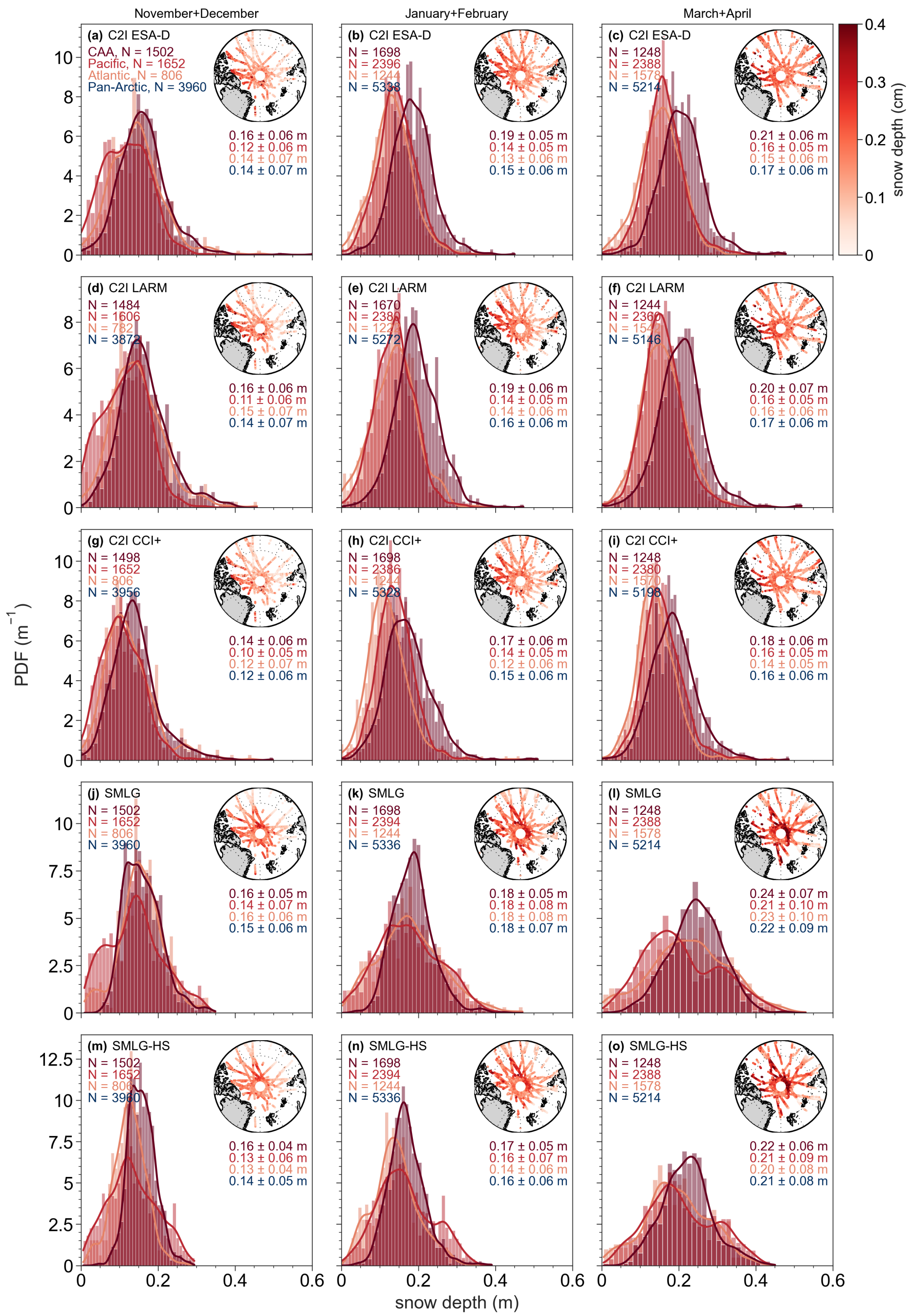

Figure 3. Bimonthly distributions of 25 km orbit-segment snow depth estimates separated by geographical areas (Figure S2): Canadian Arctic (CA), Pacific and Central Arctic (Pacific) and the Atlantic Arctic (Atlantic). Pan-Arctic statistics are provided in dark blue. Number of observations, average snow depth and standard deviation are provided. Pan-Arctic map with C2I tracks locations and corresponding snow depth are shown.

parison, Warren et al. (1999) snow depths increase by a similar ∼0.08 m for the same period over mixed ice types. CS2 both increases and decreases during the season over mixed ice types, reflecting the competition between processes of ice growth (increasing radar freeboard) and snow loading (decreasing freeboard). If the radar freeboards remained unchanged, to match SMLG accumulation over MYI the IS2 laser freeboards need to thicken by 0.14 m rather than 0.07 m over the season. In contrast, if the laser freeboards remained unchanged, to match SMLG over MYI the CS2 radar freeboards would need to reduce by 0.05 m over the winter rather than increasing by $\sim$ 0.02 m. Of course, this assumes CS2 and IS2 accurately record the true snow-ice and air-snow interface elevations, respectively. The relatively low C2I snow depth accumulation rate over MYI may also suggest that over thicker snow and older ice, the CS2 radar signal only penetrates a limited depth into the snow (Ricker et al., 2015) as potentially suggested by the along-track observations in Figure 1e. The distinction into sectors and comparison with LaKu, shows that C2I is to some extent affected by the inconsistency in data coverage which is evident when investigating accumulation rates (Figure S11). This is most prevalent for the beginning of the season in PA, where the lowest snow depths are absent in C2I, and with slightly lower snow depths over CA for C2I compared with LaKu. It is noteworthy that PA, for C2I, is more consistent between all three re-trackers, whereas larger discrepancies are observed in the two sectors, CA and AT, where high precipitation rates and sea ice deformation occurs. SMLG/SMLG-HS has a higher accumulation rate over CA, and a significantly higher accumulation rate over PA and AT, when compared to both LaKu and C2I observations. Generally, SMLG-HS has lower snow depths than SMLG, which has the largest effect over AT across the winter season, and for CA by the end of the season. Accumulation pattern of mW99 shows large variations from the other snow depth estimates, which is likely due to the application factor of 0.5 over FYI. The sensitivity of CryoSat-2 radar freeboard observations to short-term fluctuations in height following synoptic weather events has been recently documented (Nab et al., 2023).

3.4 Changes within the snow and ice pack: impacts on the radar and laser signals and backscattering horizons

To compute snow depth from the difference between freeboards, the change in speed once the radar pulse travels through the snow pack must be taken into account. This is achieved through η_s, which relies on the bulk density of snow (ρ_s). For this study, we have used a constant value of 300 kg/m^3 as often used in satellite altimetry studies (e.g., Zwally et al., 2008; Tonboe et al., 2010). Increasing ρ_s will result in an increase in η_s, which in turn will decrease the snow depth observations when following Equation (1). Investigating the impact of using different density ranges (see Figure S12 and Text S6), using the densities of Mallett et al. (2020) which are commonly used for altimetry studies (e.g., Garnier et al., 2021), we observe differences ranging from -2 to 6 mm. While the varying (ρ_s) does not have a large impact on the snow depth estimates of dual-frequency altimetry (density uncertainty of approximately 0.01 m), it has a larger impact on the conversion from freeboard to sea ice thickness when accounting for the slower wave propagation speed in snow (Mallett et al., 2020).

This methodology of dual-frequency snow depth retrieval relies on the assumption that Ku-band observations penetrate through the snow pack and are reflected at the snow-ice interface. It also relies on the assumption that laser freeboards from IS2 accurately represent the height of the mean air-snow interface elevation above sea level. While the assumption for Ku-band penetration in snow has been supported by laboratory experiments (Beaven et al., 1995), several studies have disputed that the assumption is valid for all winter and spring conditions of the Arctic sea ice pack (Tonboe et al., 2021; Stroeve et al., 2022; Nab et al., 2023; Willatt et al., 2011, 2010; King et al., 2018). Due to the high local variability of snow processes and conditions, caused by changes in atmospheric forcing, snow grain metamorphism, new precipitation, and snow redistribution in dunes, laboratory conditions of simple homogeneous snow rarely apply for the Arctic snow pack throughout a winter season. Various events like rain-on-snow (Stroeve et al., 2022), flooding of snow packs and refreezing (snow-ice formation), brine wicking (Rösel et al., 2021; Nandan et al., 2020), and more, can change the geophysical properties of the snow pack and the principal back scattering horizon that is likely to be encountered by the propagating radar signal (Stroeve et al., 2022; Tonboe et al., 2021). The study of Nab et al. (2023) presented some of the first results of synoptic variability in spaceborne altimeter-derived radar freeboards, where they suggested that in the period immediately after snow fall, radar pulses are not scattered from the snow-ice interface. An interesting future research question would therefore be to test the derived snow depth distributions for C2I samples acquired after new snowfall versus in stable conditions. Lawrence et al. (2018) used airborne observations to calibrate Ku-band CryoSat-2 and ENVISAT radar freeboards, reducing them with respect to the raw data and arguing this reduction was necessary partly due to incomplete penetration of the radar into snow. If the radar penetration needs to be corrected, it would result in an increase in C2I snow depths and potentially closer match to SMLG/SMLG-HS later in the winter. Furthermore, there are uncertainties related to the laser freeboards derived from IS2. As examples, including dark and/or specular leads in the surface classification changes the basin-scale mean laser freeboard by 0.00-0.04 m (Kwok et al., 2021) and IS2 misses a portion of ridges and rougher topography over sea ice captured by airborne laser scanner (Ricker et al., 2023). So, there is a chance that systematic uncertainty in IS2 freeboard also causes the winter C2I rates of snow accumulation to be underestimated. While several studies are currently investigating ground-based Ku- and Ka-band observations (Stroeve et al., 2020, 2022), few studies have investigated airborne dual-frequency altimetry observations over sea ice. The C2I Antarctic under-flight performed in December 2022 presents an ideal opportunity to investigate this further and interpret radar and laser freeboards obtained at satellite scales.

3.5 Comparability of C2I over sea ice

When binning observations acquired over sea ice to a similar spatial resolution, although acquired in different ways (re-tracking of waveform compared to photon-aggregated-elevation estimates), it is important to consider the expected covariance of the objectives and the ultimate objective of the study. For example, a study of basin-scale patterns in snow depth or ice topography must consider the overall conditions of the observations along 10s of km of track. Should one use the C2I observations to investigate lead-identification-capabilities or floe lengths (chord lengths) along the tracks, it is likely more important to consider a smaller search radii than used in this study to preserve information at the finest possible resolution above the noise floor. However, a smaller search radii is a compromise with the amount of data available. Furthermore, one should also consider the quality of the observations. For example, for IS2 one could argue whether weak beam observations should be included (e.g., Ricker et al. (2023) argued for the use of weak beams as the performance is comparable to that of the strong beam) or whether only strong beam observations are of high enough quality. Finally, and most importantly, one must consider at what distance or time offset the IS2 photon observations, when binned to CS2 footprint, are no longer representative of what CS2 has observed and at what cost. This affects the selection of the search radius and the amount of C2I data available, impacting the variance of the binned observations and their auto-correlation along track. Currently, we have compared smoothed C2I estimates (7 km window) or orbit-segments of 25 km, but CRISTAL requirements states snow depth estimates must be determined with low uncertainty at segments of less than or equal to 25 km. So, whilst the CS2 raw sampling rate is unrealistic due to the speckle noise of CS2, we are ought to consider at what sampling rate the snow depth variability starts to be realistic. A comparison with airborne under-flights will allow for further investigation of the length scales at which snow depth can be retrieved from space with reasonable accuracy.

4 Conclusions

Here, we present a first examination of near-coincident radar (CS2) and laser (IS2) altimetry observations obtained through the C2I campaign. From the C2I orbits, we bin IS2 to CS2's sampling rate (20 Hz) using a search radius of 3500 m (for both CS2 and IS2) to include as many IS2 points as possible. Due to uncertainty estimates not being provided in the products, we can only discuss precision of the C2I snow depth estimates in relation to CRISTAL requirements. The C2I observations shows similar precision (here used as proxy for uncertainty) computed using standard deviation along $\sim$ 500 km tracks at scales of $\sim$7 and 25 km (less than 0.05 m), which are within the CRISTAL requirements of uncertainty. More work is necessary to fully evaluate the uncertainty of these snow depth estimates. The C2I snow depths show a clear seasonal accumulation over FYI, matching the accumulation predicted by reanalysis precipitation. However, over MYI there is minimal accumulation, reflecting a relatively slow thickening of both IS2 and CS2 freeboards over MYI for the C2I orbits. This highlights the possibility that Ku-band radar signals are not penetrating to the snow-ice interface over MYI, which we further investigated by comparing with available in situ snow depth observations from drifting buoys. Even though, there is a major lack of reference data, the C2I snow depths tend to be underestimated when compared to AWI acoustic buoy data, whereas the seasonal accumulation was captured well when compared to SIMBA thermistor-string buoys deployed on level ice. Recent airborne campaigns will be critical for meeting the gap in reference snow depth observations over sea ice. This study shows the potential for the valuable high-resolution along-track snow depth observations to be acquired by the dual-frequency CRISTAL mission.

5 Open Research

Data used and produced in this study is available from `https://figshare.com/s/8e4a1134bfc99dd2d535` (last access: 2023/05/265) at Data DTU via doi:10.11583/DTU.21369129 (link shall become active once the data submission has been reviewed by Data DTU) (Fredensborg Hansen, 2023), and the code is available on `https://github.com/reneefredensborg/CRYO2ICE_freeboards_snow_depths_roughness_auxiliary_v1` (last access: 2023/05/25). CS2 Baseline-D L1b and L2 products along with IS2 ATL10 products were retrieved through the `www.cryo2ice.org` (last access: 2022/03/02) tool (now known as `www.cs2eo.org`, last access: 2022/10/13), where the code for retrieval (provided by the tool) of the data is available at: `https://github.com/reneefredensborg/CRYO2ICE_freeboards_snow_depths_roughness_auxiliary_v1/blob/main/notebooks/Download_data_using_CRYO2ICE_tool.ipynb` (last access: 2023/05/28). CS2 LARM radar freeboard product was provided by JCL (Landy et al., 2020), along with gridded LARM and IS2 observations (all available from doi:10.11583/DTU.21369129 as part of this study's data package). CS2 CCI+ radar freeboards are available from `ftp://ftp.awi.de/sea_ice/projects/cci/crdp/v3p0-rc1/cryosat2/nh/l2p_trajectory/` (last access: 2022/10/25) (Rinne & Hendricks, 2023; Hendricks et al., 2023), and the gridded products are available from `ftp://ftp.awi.de/sea_ice/projects/cci/crdp/v3p0-rc1/cryosat2/nh/l3c_grid/` (last access: 2023/05/24). Passive-microwave product is available at the National Snow and Ice Data Center (NSIDC) as AMSR-E/AMSR2 Unified L3 Daily 12.5 km Brightness Temperatures, Sea Ice Concentration, Motion & Snow Depth Polar Grids, Version 1 (AU_SI12) (Meier et al., 2018), last access: 2022/10/12. SMLG product is available at NSIDC as Lagrangian Snow Distributions for Sea-Ice Applications, Version 1 (NSIDC-0758) (Liston et al., 2021), last access: 2022/10/12, and SMLG-HS is available at http://doi.org/10.23728/fmi-b2share.321122c5c72245c892364b6b933e8982 (Merkouriadi & Liston, 2022), where an update including winter 2020-2021 was provided by IM. Autonomous sea ice measurements (snow depth buoys from AWI) from 2020/10/01 to 2021/04/30 were obtained from `https://www.meereisportal.de` (grant: REKLIM-2013-04) with doi:10.1594/PANGAEA.875638 (Nicolaus et al., 2021). SIMBA buoy snow depths were provided by Rubio Lei.

Acknowledgments

RMFH acknowledges support through travel grants from UArctic North2North, P.A. Fisker's Fond, Thomas B. Thriges Fond, IDAs and Berg-Nielsens Studie- og støttefond, and Niels Bohr Fonden during research stays at UNIS, where part of this work was conducted. RMFH and HSK acknowledges support from Cryo2IceEx under grant nr. 4000128488/19/NL/FF/gp CCN. JCL acknowledges support from the CIRFA project under grant nr. 237906 and the INTERAAC project under grant nr. 328957 from the Research Council of Norway (RCN). JCL and ER acknowledges support from the Fram Centre program for Sustainable Development of the Arctic Ocean (SUDARCO) under grant nr. 2551323. IM, ER, and HSK was supported by the ESA grant CCI+ 4000126449/19/I-NB. IM also acknowledges support from the CROS-Arctic project with grant nr. 341550 by the Academy of Finland. We thank Rubio Lei and Bin Cheng for discussions regarding SIMBA buoy observations and for providing snow depth estimates from said buoys.

References

Alford, J., Ewart, M., Bizon, J., Easthope, R., Gourmelen, N., Parrinello, T., ... Meloni, M. (2021). *CRYO2ICE Coincident Data Explorer, Version 1.* `http://cryo2ice.org.` (European Space Agency, accessed: 3/3/2022)

Armitage, T. W. K., & Davidson, M. W. J. (2014). Using the interferometric capabilities of the esa cryosat-2 mission to improve the accuracy of sea ice freeboard retrievals. *IEEE Transactions on Geoscience and Remote Sensing*, *52*(1), 529-536. doi: 10.1109/TGRS.2013.2242082

Bagnardi, M., Kurtz, N. T., Petty, A. A., & Kwok, R. (2021). Sea Surface Height Anomalies of the Arctic Ocean From ICESat-2: A First Examination and Comparisons With CryoSat-2. *Geophysical Research Letters*, *48*(14), e2021GL093155. doi: https://doi.org/10.1029/2021GL093155

Beaven, S. G., Lockhart, G. L., Gogineni, S. P., Hossetnmostafa, A. R., Jezek, K., Gow, A. J., ... Tjuatja, S. (1995). Laboratory measurements of radar backscatter from bare and snow-covered saline ice sheets. *International Journal of Remote Sensing*, *16*(5), 851-876. doi: 10.1080/01431169508954448

Fredensborg Hansen, R. M. (2023). *Cryo2ice radar/laser freeboards, snow depth on sea ice and comparison against auxiliary data during winter season 2020-2021 (version 1) [dataset].* Technical University of Denmark. doi: 10.11583/DTU.21369129

Fredensborg Hansen, R. M., Rinne, E., Farrell, S. L., & Skourup, H. (2021). Estimation of degree of sea ice ridging in the bay of bothnia based on geolocated photon heights from icesat-2. *The Cryosphere*, *15*(6), 2511–2529. Retrieved from `https://tc.copernicus.org/articles/15/2511/2021/` doi: 10.5194/tc-15-2511-2021

Garnier, F., Fleury, S., Garric, G., Bouffard, J., Tsamados, M., Laforge, A., ... Remy, F. (2021). Advances in altimetric snow depth estimates using bi-frequency saral and cryosat-2 ka–ku measurements. *The Cryosphere*, *15*(12), 5483–5512. Retrieved from `https://tc.copernicus.org/articles/15/5483/2021/` doi: 10.5194/tc-15-5483-2021

Giles, K., Laxon, S., Wingham, D., Wallis, D., Krabill, W., Leuschen, C., ... Raney, R. (2007). Combined airborne laser and radar altimeter measurements over the Fram Strait in May 2002. *Remote Sensing of Environment*, *111*(2), 182-194. (Remote Sensing of the Cryosphere Special Issue) doi: https://doi.org/10.1016/j.rse.2007.02.037

Grosfeld, K., Treffeisen, R., Asseng, J., Bartsch, A., Bräuer, B., Fritzsch, B., ... Weigelt, M. (2016). Online sea-ice knowledge and data platform ¡www.meereisportal.de¿. *Polarforschung*, *85*(2), 143-155. doi: doi:10.2312/polfor.2016.011

Guerreiro, K., Fleury, S., Zakharova, E., Rémy, F., & Kouraev, A. (2016). Potential for estimation of snow depth on arctic sea ice from cryosat-2 and saral/altika missions. *Remote Sensing of Environment*, *186*, 339-349. Retrieved from `https://www.sciencedirect.com/science/article/pii/S0034425716302711` doi: https://doi.org/10.1016/j.rse.2016.07.013

Hendricks, S., Paul, S., & Rinne, E. (2023). *ESA Sea Ice Climate Change Initiative (Sea_Ice_cci): Northern hemisphere sea ice thickness from CryoSat-2 on the satellite swath (L2P), v2.0.* (Reference D4.2, Phase 1) doi: 10.5285/5b6033bfb7f241e89132a83fdc3d5364

Hendricks, S., & Ricker, R. (2020). *User Guide and Algorithm Specification – AWI CryoSat-2 Sea Ice Thickness (version 2.3).* Available at: `https://epic.awi.de/id/eprint/53331/1/AWI-CryoSat2-ProductUserGuide-v2p3.pdf` (Accessed 04 March 2020).

Jackson, K., Wilkinson, J., Maksym, T., Meldrum, D., Beckers, J., Haas, C., & Mackenzie, D. (2013). A novel and low-cost sea ice mass balance buoy. *Journal of Atmospheric and Oceanic Technology*, *30*(11), 2676 - 2688. Retrieved from `https://journals.ametsoc.org/view/journals/atot/30/11/jtech-d-13-00058_1.xml` doi: https://doi.org/10.1175/JTECH-D-13-00058.1

Kacimi, S., & Kwok, R. (2020). The antarctic sea ice cover from icesat-2 and cryosat-2: freeboard, snow depth, and ice thickness. *The Cryosphere*, *14*(12), 4453–4474. Retrieved from `https://tc.copernicus.org/articles/14/4453/2020/` doi: 10.5194/tc-14-4453-2020

Kacimi, S., & Kwok, R. (2022). Arctic snow depth, ice thickness, and volume from icesat-2 and cryosat-2: 2018–2021. *Geophysical Research Letters*, *49*(5), e2021GL097448. Retrieved from `https://agupubs.onlinelibrary.wiley.com/doi/abs/10.1029/2021GL097448` (e2021GL097448 2021GL097448) doi: https://doi.org/10.1029/2021GL097448

Kern, M., Cullen, R., Berruti, B., Bouffard, J., Casal, T., Drinkwater, M. R., . . . Yackel, J. (2020). The copernicus polar ice and snow topography altimeter (cristal) high-priority candidate mission. *The Cryosphere*, *14*(7), 2235–2251. Retrieved from `https://tc.copernicus.org/articles/14/2235/2020/` doi: 10.5194/tc-14-2235-2020

King, J., Howell, S., Brady, M., Toose, P., Derksen, C., Haas, C., & Beckers, J. (2020). Local-scale variability of snow density on arctic sea ice. *The Cryosphere*, *14*(12), 4323–4339. Retrieved from `https://tc.copernicus.org/articles/14/4323/2020/` doi: 10.5194/tc-14-4323-2020

King, J., Skourup, H., Hvidegaard, S. M., Rösel, A., Gerland, S., Spreen, G., . . . Liston, G. E. (2018). Comparison of freeboard retrieval and ice thickness calculation from als, asiras, and cryosat-2 in the norwegian arctic to field measurements made during the n-ice2015 expedition. *Journal of Geophysical Research: Oceans*, *123*(2), 1123-1141. doi: https://doi.org/10.1002/2017JC013233

Kurtz, N. T., & Farrell, S. L. (2011). Large-scale surveys of snow depth on arctic sea ice from operation icebridge. *Geophysical Research Letters*, *38*(20). doi: https://doi.org/10.1029/2011GL049216

Kwok, R., Kacimi, S., Webster, M., Kurtz, N., & Petty, A. (2020). Arctic snow depth and sea ice thickness from icesat-2 and cryosat-2 freeboards: A first examination. *Journal of Geophysical Research: Oceans*, *125*(3), e2019JC016008. doi: https://doi.org/10.1029/2019JC016008

Kwok, R., Petty, A., Bagnardi, M., Wimert, J. T., Cunningham, G. F., Hancock, D. W., & andNathan Kurtz, A. I. (2022). *ICE, CLOUD, and Land Elevation Satellite (ICESat-2) Project: Algorithm Theoretical Basis Document (ATBD) For Sea Ice Products (ATL07/ATL10/ATL20/ATL21) Release 005.* Available at: `https://nsidc.org/sites/default/files/icesat2_atl07_atl10_atl20_atl21_atbd_r005_1.pdf` (Accessed 24 May 2023).

Kwok, R., Petty, A. A., Bagnardi, M., Kurtz, N. T., Cunningham, G. F., Ivanoff, A.,

& Kacimi, S. (2021). Refining the sea surface identification approach for determining freeboards in the icesat-2 sea ice products. *The Cryosphere*, *15*(2), 821–833. Retrieved from https://tc.copernicus.org/articles/15/821/2021/ doi: 10.5194/tc-15-821-2021

Landy, J. C., Petty, A. A., Tsamados, M., & Stroeve, J. C. (2020). Sea ice roughness overlooked as a key source of uncertainty in cryosat-2 ice freeboard retrievals. *Journal of Geophysical Research: Oceans*, *125*(5), e2019JC015820. doi: https://doi.org/10.1029/2019JC015820

Landy, J. C., Tsamados, M., & Scharien, R. K. (2019). A Facet-Based Numerical Model for Simulating SAR Altimeter Echoes From Heterogeneous Sea Ice Surfaces. *IEEE Transactions on Geoscience and Remote Sensing*, *57*(7), 4164-4180. doi: 10.1109/TGRS.2018.2889763

Launiainen, J., & Cheng, B. (1998). Modelling of ice thermodynamics in natural water bodies. *Cold Regions Science and Technology*, *27*(3), 153-178. doi: https://doi.org/10.1016/S0165-232X(98)00009-3

Lawrence, I. R., Tsamados, M. C., Stroeve, J. C., Armitage, T. W. K., & Ridout, A. L. (2018). Estimating snow depth over arctic sea ice from calibrated dual-frequency radar freeboards. *The Cryosphere*, *12*(11), 3551–3564. Retrieved from https://tc.copernicus.org/articles/12/3551/2018/ doi: 10.5194/tc-12-3551-2018

Lei, R., Cheng, B., Hoppmann, M., & Zuo, G. (2021). *Snow depth and sea ice thickness derived from the measurements of SIMBA buoys deployed in the Arctic Ocean during the Legs 1a, 1, and 3 of the MOSAiC campaign in 2019-2020* [data set]. PANGAEA. Retrieved from https://doi.org/10.1594/PANGAEA.938244 doi: 10.1594/PANGAEA.938244

Leppäranta, M. (1983, 04). A Growth Model for Black Ice, Snow Ice and Snow Thickness in Subarctic Basins. *Hydrology Research*, *14*(2), 59-70. Retrieved from https://doi.org/10.2166/nh.1983.0006 doi: 10.2166/nh.1983.0006

Liao, Z., Cheng, B., Zhao, J., Vihma, T., Jackson, K., Yang, Q., ... Cheng, X. (2019). Snow depth and ice thickness derived from simba ice mass balance buoy data using an automated algorithm. *International Journal of Digital Earth*, *12*(8), 962-979. doi: 10.1080/17538947.2018.1545877

Liston, G. E., Itkin, P., Stroeve, J., Tschudi, M., Stewart, J. S., Pedersen, S. H., ... Elder, K. (2020). A lagrangian snow-evolution system for sea-ice applications (snowmodel-lg): Part i—model description. *Journal of Geophysical Research: Oceans*, *125*(10), e2019JC015913. doi: https://doi.org/10.1029/2019JC015913

Liston, G. E., Polashenski, C., Rösel, A., Itkin, P., King, J., Merkouriadi, I., & Haapala, J. (2018). A distributed snow-evolution model for sea-ice applications (snowmodel). *Journal of Geophysical Research: Oceans*, *123*(5), 3786-3810. doi: https://doi.org/10.1002/2017JC013706

Liston, G. E., Stroeve, J., & Itkin., P. (2021). *"lagrangian snow distributions for sea-ice applications, version 1"*. NASA National Snow and Ice Data Center Distributed Active Archive Center. Retrieved from https://nsidc.org/data/NSIDC-0758/versions/1 doi: 10.5067/27A0P5M6LZBI

Magruder, L. A., Brunt, K. M., & Alonzo, M. (2020). Early ICESat-2 on-orbit Geolocation Validation Using Ground-Based Corner Cube Retro-Reflectors. *Remote Sensing*, *12*(21). doi: 10.3390/rs12213653

Mallett, R. D. C., Lawrence, I. R., Stroeve, J. C., Landy, J. C., & Tsamados, M. (2020). Brief communication: Conventional assumptions involving the speed of radar waves in snow introduce systematic underestimates to sea ice thickness and seasonal growth rate estimates. *The Cryosphere*, *14*(1), 251–260. Retrieved from https://tc.copernicus.org/articles/14/251/2020/ doi: 10.5194/tc-14-251-2020

Markus, T., & Cavalieri, D. (2000). An enhancement of the nasa team sea ice algorithm. *IEEE Transactions on Geoscience and Remote Sensing*, *38*(3), 1387-1398. doi: 10.1109/36.843033

Markus, T., & Cavalieri, D. J. (1998). Snow depth distribution over sea ice in the southern ocean from satellite passive microwave data. In M. O. Jeffries (Ed.), *Antarctic sea ice: Physical processes, interactions and variability, antarct. res. ser.* (Vol. 74, pp. 19–39). Washington, D.C.: AGU.

Markus, T., & Cavalieri, D. J. (2009). "the amsr-e nt2 sea ice concentration algorithm: its basis and implementation". *Journal of The Remote Sensing Society of Japan*, *29*(1), 216-225. doi: 10.11440/rssj.29.216

Meier, W. N., Markus, T., & Comiso., J. C. (2018). *"amsr-e/amsr2 unified l3 daily 12.5 km brightness temperatures, sea ice concentration, motion & snow depth polar grids, version 1".* NASA National Snow and Ice Data Center Distributed Active Archive Center. Retrieved from `https://nsidc.org/data/AU_SI12/versions/1` doi: 10.5067/RA1MIJOYPK3P

Meloni, M., Bouffard, J., Parrinello, T., Dawson, G., Garnier, F., Helm, V., ... Mizzi, L. (2020). CryoSat Ice Baseline-D validation and evolutions. *The Cryosphere*, *14*(6), 1889–1907. doi: 10.5194/tc-14-1889-2020

Merkouriadi, I., & Liston, G. (2022). *Quantifying pan-arctic snow depth and density trends caused by snow-ice formation [dataset].* Finnish Meteorological Institute. Retrieved from `https://fmi.b2share.csc.fi/records/321122c5c72245c892364b6b933e8982` doi: 10.23728/FMI-B2SHARE.321122C5C72245C892364B6B933E8982

Merkouriadi, I., Liston, G. E., Graham, R. M., & Granskog, M. A. (2020). Quantifying the potential for snow-ice formation in the arctic ocean. *Geophysical Research Letters*, *47*(4), e2019GL085020. Retrieved from `https://agupubs.onlinelibrary.wiley.com/doi/abs/10.1029/2019GL085020` (e2019GL085020 2019GL085020) doi: https://doi.org/10.1029/2019GL085020

Moon, W., Nandan, V., Scharien, R. K., Wilkinson, J., Yackel, J. J., Barrett, A., ... Mahmud, M. (2019). Physical length scales of wind-blown snow redistribution and accumulation on relatively smooth arctic first-year sea ice. *Environmental Research Letters*, *14*(10), 260-273. doi: 10.1088/1748-9326/ab3b8d

Nab, C., Mallett, R., Gregory, W., Landy, J., Lawrence, I., Willatt, R., ... Tsamados, M. (2023). Synoptic variability in satellite altimeter-derived radar freeboard of arctic sea ice. *Geophysical Research Letters*, *50*(2), e2022GL100696. doi: https://doi.org/10.1029/2022GL100696

Nandan, V., Geldsetzer, T., Yackel, J., Mahmud, M., Scharien, R., Howell, S., ... Else, B. (2017). Effect of snow salinity on cryosat-2 arctic first-year sea ice freeboard measurements. *Geophysical Research Letters*, *44*(20), 10,419-10,426. doi: https://doi.org/10.1002/2017GL074506

Nandan, V., Scharien, R. K., Geldsetzer, T., Kwok, R., Yackel, J. J., Mahmud, M. S., ... Frey, M. (2020). Snow property controls on modeled ku-band altimeter estimates of first-year sea ice thickness: Case studies from the canadian and norwegian arctic. *IEEE Journal of Selected Topics in Applied Earth Observations and Remote Sensing*, *13*, 1082-1096. doi: 10.1109/JSTARS.2020.2966432

Neumann, T. A., Martino, A. J., Markus, T., Bae, S., Bock, M. R., Brenner, A. C., ... Thomas, T. C. (2019). The Ice, Cloud, and Land Elevation Satellite – 2 mission: A global geolocated photon product derived from the Advanced Topographic Laser Altimeter System. *Remote Sensing of Environment*, *233*, 111325. doi: https://doi.org/10.1016/j.rse.2019.111325

Nicolaus, M., Hoppmann, M., Arndt, S., Hendricks, S., Katlein, C., Nicolaus, A., ... Schwegmann, S. (2021). Snow depth and air temperature seasonality on sea ice derived from snow buoy measurements. *Frontiers in Marine Science*, *8*. Retrieved from `https://www.frontiersin.org/articles/10.3389/fmars.2021.655446` doi: 10.3389/fmars.2021.655446

Perovich, D., Richter-Menge, J., & Polashenksi, C. (2023). *Observing and understanding climate change: Monitoring the mass balance, motion, and thickness of Arctic sea ice.* available at: `http://imb-crrel-dartmouth.org`. (last access: 2023/02/15)

Petty, A. A., Bagnardi, M., Kurtz, N. T., Tilling, R., Fons, S., Armitage, T., ... Kwok, R. (2021). Assessment of icesat-2 sea ice surface classification with sentinel-2 imagery: Implications for freeboard and new estimates of lead and floe geometry. *Earth and Space Science*, *8*(3), e2020EA001491. doi: https://doi.org/10.1029/2020EA001491

Ricker, R., Fons, S., Jutila, A., Hutter, N., Duncan, K., Farrell, S. L., ... Fredensborg Hansen, R. M. (2023). Linking scales of sea ice surface topography: evaluation of icesat-2 measurements with coincident helicopter laser scanning during mosaic. *The Cryosphere*, *17*(3), 1411–1429. Retrieved from `https://tc.copernicus.org/articles/17/1411/2023/` doi: 10.5194/tc-17-1411-2023

Ricker, R., Hendricks, S., Perovich, D. K., Helm, V., & Gerdes, R. (2015). Impact of snow accumulation on cryosat-2 range retrievals over arctic sea ice: An observational approach with buoy data. *Geophysical Research Letters*, *42*(11), 4447-4455. Retrieved from `https://agupubs.onlinelibrary.wiley.com/doi/abs/10.1002/2015GL064081` doi: https://doi.org/10.1002/2015GL064081

Rinne, E., & Hendricks, S. (2023). *CCI+ Sea Ice ECV Sea Ice Thickness Product User Guide (PUG) .* (Reference D4.2, Phase 1)

Rösel, A., Farrell, S. L., Nandan, V., Richter-Menge, J., Spreen, G., Divine, D. V., ... Gerland, S. (2021). Implications of surface flooding on airborne estimates of snow depth on sea ice. *The Cryosphere*, *15*(6), 2819–2833. Retrieved from `https://tc.copernicus.org/articles/15/2819/2021/` doi: 10.5194/tc-15-2819-2021

Rostosky, P., Spreen, G., Farrell, S. L., Frost, T., Heygster, G., & Melsheimer, C. (2018). Snow depth retrieval on arctic sea ice from passive microwave radiometers—improvements and extensions to multiyear ice using lower frequencies. *Journal of Geophysical Research: Oceans*, *123*(10), 7120-7138. doi: https://doi.org/10.1029/2018JC014028

Stroeve, J., Nandan, V., Willatt, R., Dadic, R., Rotosky, P., Gallagher, M., ... Schneebeli, M. (2022). Rain-on-snow (ros) understudied in sea ice remote sensing: A multi-sensor analysis of ros during mosaic. *The Cryosphere Discussions*, *2022*, 1–42. doi: 10.5194/tc-2021-383

Stroeve, J., Nandan, V., Willatt, R., Tonboe, R., Hendricks, S., Ricker, R., ... Tsamados, M. (2020). Surface-based ku- and ka-band polarimetric radar for sea ice studies. *The Cryosphere*, *14*(12), 4405–4426. Retrieved from `https://tc.copernicus.org/articles/14/4405/2020/` doi: 10.5194/tc-14-4405-2020

Sturm, M., Holmgren, J., & Perovich, D. K. (2002). Winter snow cover on the sea ice of the arctic ocean at the surface heat budget of the arctic ocean (sheba): Temporal evolution and spatial variability. *Journal of Geophysical Research: Oceans*, *107*(C10), SHE 23-1-SHE 23-17. doi: https://doi.org/10.1029/2000JC000400

Tonboe, R. T., Nandan, V., Yackel, J., Kern, S., Toudal Pedersen, L., & Stroeve, J. (2021). Simulated Ka-and Ku-band radar altimeter height and freeboard estimation on snow-covered Arctic sea ice. *Cryosphere*, *15*(4), 1811–1822. doi: 10.5194/tc-15-1811-2021

Tonboe, R. T., Pedersen, L. T., & Haas, C. (2010). Simulation of the cryosat-2 satellite radar altimeter sea ice thickness retrieval uncertainty. *Canadian Journal of Remote Sensing*, *36*(1), 55-67. doi: 10.5589/m10-027

Ulaby, F., Moore, R. K., & Fung, A. K. (1986). *Microwave remote sensing: From theory to applications (vol. 3).* Artech House: Norwood, MA.

Vivier, F., & Lourenco, A. (2023). *Sea ice thickness and ancillary parameters between the North Pole and Fram Strait from the Ice-T buoy.* available from SEANOE at: `https://www.seanoe.org/data/00766/87766/`, doi: 10.17882/87766. (last access: 2023/02/16)

Warren, S. G., Rigor, I. G., Untersteiner, N., Radionov, V. F., Bryazgin, N. N., Aleksandrov, Y. I., & Colony, R. (1999). Snow depth on arctic sea ice. *Journal of Climate*, *12*(6), 1814–1829. doi: 10.1175/1520-0442(1999)012\⟨1814:SDOASI\⟩2.0.CO;2

Webster, M., Gerland, S., Holland, M., Hunke, E. C., Kwok, R., Lecomte, O., ... Sturm, M. (2018). Snow in the changing sea-ice system. *Nature Climate Change*, *8*(11). Retrieved from `https://www.osti.gov/biblio/1525848` doi: 10.1038/s41558-018-0286-7

Willatt, R., Giles, K., Laxon, S., Stone-Drake, L., & Worby, A. (2010). Field investigations of ku-band radar penetration into snow cover on antarctic sea ice. *IEEE Transactions on Geoscience and Remote Sensing*, *48*(1), 365-372. doi: 10.1109/TGRS.2009.2028237

Willatt, R., Laxon, S., Giles, K., Cullen, R., Haas, C., & Helm, V. (2011). Ku-band radar penetration into snow cover on arctic sea ice using airborne data. *Annals of Glaciology*, *52*(57), 197–205. doi: 10.3189/172756411795931589

Zhou, L., Stroeve, J., Xu, S., Petty, A., Tilling, R., Winstrup, M., ... Nandan, V. (2021). Inter-comparison of snow depth over arctic sea ice from reanalysis reconstructions and satellite retrieval. *The Cryosphere*, *15*(1), 345–367. Retrieved from `https://tc.copernicus.org/articles/15/345/2021/` doi: 10.5194/tc-15-345-2021

Zwally, H. J., Yi, D., Kwok, R., & Zhao, Y. (2008). Icesat measurements of sea ice freeboard and estimates of sea ice thickness in the weddell sea. *Journal of Geophysical Research: Oceans*, *113*(C2). doi: https://doi.org/10.1029/2007JC004284

Figure 1.

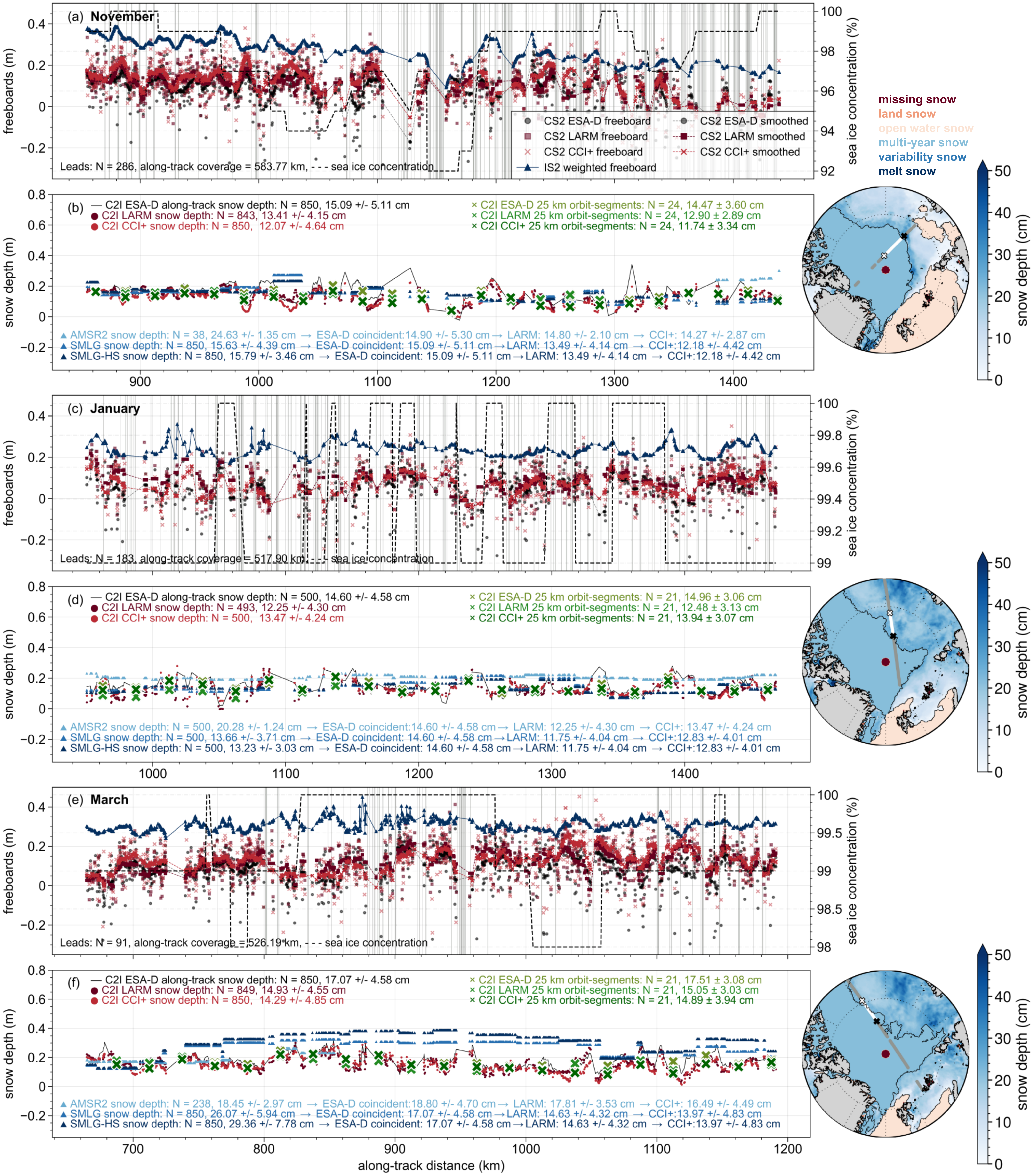

(a) November
freeboards (m)
sea ice concentration (%)
CS2 ESA-D freeboard
CS2 LARM freeboard
CS2 CCI+ freeboard
IS2 weighted freeboard
CS2 ESA-D smoothed
CS2 LARM smoothed
CS2 CCI+ smoothed
Leads: N = 286, along-track coverage = 583.77 km, - - - sea ice concentration
missing snow
land snow
open water snow
multi-year snow
variability snow
melt snow
(b)
— C2I ESA-D along-track snow depth: N = 850, 15.09 +/- 5.11 cm
C2I LARM snow depth: N = 843, 13.41 +/- 4.15 cm
C2I CCI+ snow depth: N = 850, 12.07 +/- 4.64 cm
× C2I ESA-D 25 km orbit-segments: N = 24, 14.47 ± 3.60 cm
× C2I LARM 25 km orbit-segments: N = 24, 12.90 ± 2.89 cm
× C2I CCI+ 25 km orbit-segments: N = 24, 11.74 ± 3.34 cm
snow depth (m)
AMSR2 snow depth: N = 38, 24.63 +/- 1.35 cm → ESA-D coincident:14.90 +/- 5.30 cm → LARM: 14.80 +/- 2.10 cm → CCI+: 14.27 +/- 2.87 cm
SMLG snow depth: N = 850, 15.63 +/- 4.39 cm → ESA-D coincident: 15.09 +/- 5.11 cm → LARM: 13.49 +/- 4.14 cm → CCI+:12.18 +/- 4.42 cm
SMLG-HS snow depth: N = 850, 15.79 +/- 3.46 cm → ESA-D coincident: 15.09 +/- 5.11 cm → LARM: 13.49 +/- 4.14 cm → CCI+:12.18 +/- 4.42 cm
snow depth (cm)
(c) January
Leads: N = 183, along-track coverage = 517.90 km, - - - sea ice concentration
(d)
— C2I ESA-D along-track snow depth: N = 500, 14.60 +/- 4.58 cm
C2I LARM snow depth: N = 493, 12.25 +/- 4.30 cm
C2I CCI+ snow depth: N = 500, 13.47 +/- 4.24 cm
× C2I ESA-D 25 km orbit-segments: N = 21, 14.96 ± 3.06 cm
× C2I LARM 25 km orbit-segments: N = 21, 12.48 ± 3.13 cm
× C2I CCI+ 25 km orbit-segments: N = 21, 13.94 ± 3.07 cm
AMSR2 snow depth: N = 500, 20.28 +/- 1.24 cm → ESA-D coincident:14.60 +/- 4.58 cm → LARM: 12.25 +/- 4.30 cm → CCI+: 13.47 +/- 4.24 cm
SMLG snow depth: N = 500, 13.66 +/- 3.71 cm → ESA-D coincident: 14.60 +/- 4.58 cm → LARM: 11.75 +/- 4.04 cm → CCI+:12.83 +/- 4.01 cm
SMLG-HS snow depth: N = 500, 13.23 +/- 3.03 cm → ESA-D coincident: 14.60 +/- 4.58 cm → LARM: 11.75 +/- 4.04 cm → CCI+:12.83 +/- 4.01 cm
(e) March
Leads: N = 91, along-track coverage = 526.19 km, - - - sea ice concentration
(f)
— C2I ESA-D along-track snow depth: N = 850, 17.07 +/- 4.58 cm
C2I LARM snow depth: N = 849, 14.93 +/- 4.55 cm
C2I CCI+ snow depth: N = 850, 14.29 +/- 4.85 cm
× C2I ESA-D 25 km orbit-segments: N = 21, 17.51 ± 3.08 cm
× C2I LARM 25 km orbit-segments: N = 21, 15.05 ± 3.03 cm
× C2I CCI+ 25 km orbit-segments: N = 21, 14.89 ± 3.94 cm
AMSR2 snow depth: N = 238, 18.45 +/- 2.97 cm → ESA-D coincident:18.80 +/- 4.70 cm → LARM: 17.81 +/- 3.53 cm → CCI+: 16.49 +/- 4.49 cm
SMLG snow depth: N = 850, 26.07 +/- 5.94 cm → ESA-D coincident: 17.07 +/- 4.58 cm → LARM: 14.63 +/- 4.32 cm → CCI+:13.97 +/- 4.83 cm
SMLG-HS snow depth: N = 850, 29.36 +/- 7.78 cm → ESA-D coincident: 17.07 +/- 4.58 cm → LARM: 14.63 +/- 4.32 cm → CCI+:13.97 +/- 4.83 cm
along-track distance (km)

Figure 2.

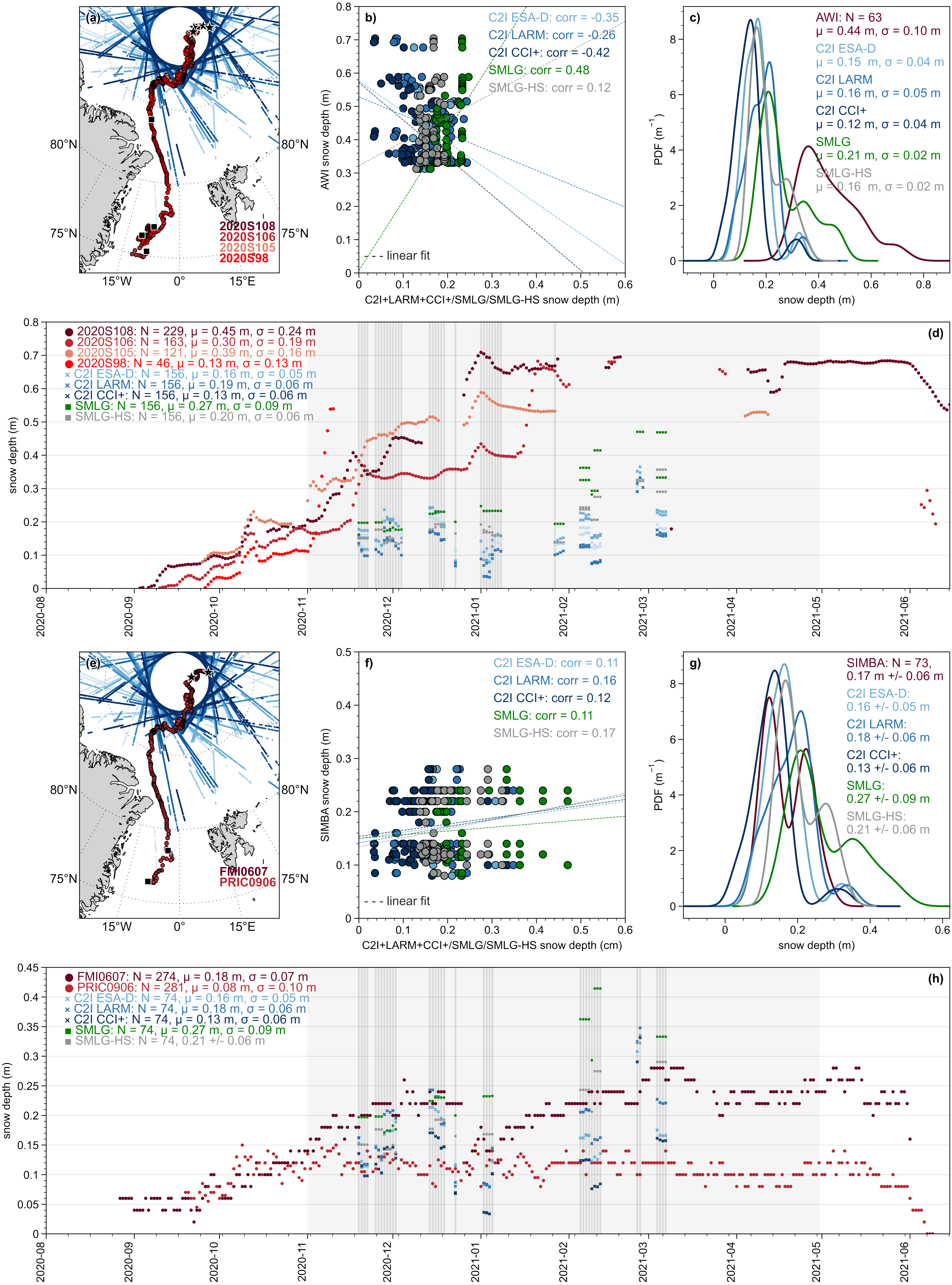

(a)
80°N
75°N
15°W
0°
15°E
2020S108
2020S106
2020S105
2020S98
b)
C2I ESA-D: corr = -0.35
C2I LARM: corr = -0.26
C2I CCI+: corr = -0.42
SMLG: corr = 0.48
SMLG-HS: corr = 0.12
AWI snow depth (m)
- - - linear fit
C2I+LARM+CCI+/SMLG/SMLG-HS snow depth (m)
c)
AWI: N = 63
μ = 0.44 m, σ = 0.10 m
C2I ESA-D
μ = 0.15 m, σ = 0.04 m
C2I LARM
μ = 0.16 m, σ = 0.05 m
C2I CCI+
μ = 0.12 m, σ = 0.04 m
SMLG
μ = 0.21 m, σ = 0.02 m
SMLG-HS
μ = 0.16 m, σ = 0.02 m
PDF (m^-1)
snow depth (m)
(d)
2020S108: N = 229, μ = 0.45 m, σ = 0.24 m
2020S106: N = 163, μ = 0.30 m, σ = 0.19 m
2020S105: N = 121, μ = 0.39 m, σ = 0.16 m
2020S98: N = 46, μ = 0.13 m, σ = 0.13 m
C2I ESA-D: N = 156, μ = 0.16 m, σ = 0.05 m
C2I LARM: N = 156, μ = 0.19 m, σ = 0.06 m
C2I CCI+: N = 156, μ = 0.13 m, σ = 0.06 m
SMLG: N = 156, μ = 0.27 m, σ = 0.09 m
SMLG-HS: N = 156, μ = 0.20 m, σ = 0.06 m
snow depth (m)
2020-08
2020-09
2020-10
2020-11
2020-12
2021-01
2021-02
2021-03
2021-04
2021-05
2021-06
(e)
80°N
75°N
15°W
0°
15°E
FMI0607
PRIC0906
f)
C2I ESA-D: corr = 0.11
C2I LARM: corr = 0.16
C2I CCI+: corr = 0.12
SMLG: corr = 0.11
SMLG-HS: corr = 0.17
SIMBA snow depth (m)
- - - linear fit
C2I+LARM+CCI+/SMLG/SMLG-HS snow depth (cm)
g)
SIMBA: N = 73,
0.17 m +/- 0.06 m
C2I ESA-D:
0.16 +/- 0.05 m
C2I LARM:
0.18 +/- 0.06 m
C2I CCI+:
0.13 +/- 0.06 m
SMLG:
0.27 +/- 0.09 m
SMLG-HS:
0.21 +/- 0.06 m
PDF (m^-1)
snow depth (m)
(h)
FMI0607: N = 274, μ = 0.18 m, σ = 0.07 m
PRIC0906: N = 281, μ = 0.08 m, σ = 0.10 m
C2I ESA-D: N = 74, μ = 0.16 m, σ = 0.05 m
C2I LARM: N = 74, μ = 0.18 m, σ = 0.06 m
C2I CCI+: N = 74, μ = 0.13 m, σ = 0.06 m
SMLG: N = 74, μ = 0.27 m, σ = 0.09 m
SMLG-HS: N = 74, 0.21 +/- 0.06 m
snow depth (m)
2020-08
2020-09
2020-10
2020-11
2020-12
2021-01
2021-02
2021-03
2021-04
2021-05
2021-06

Figure 3.

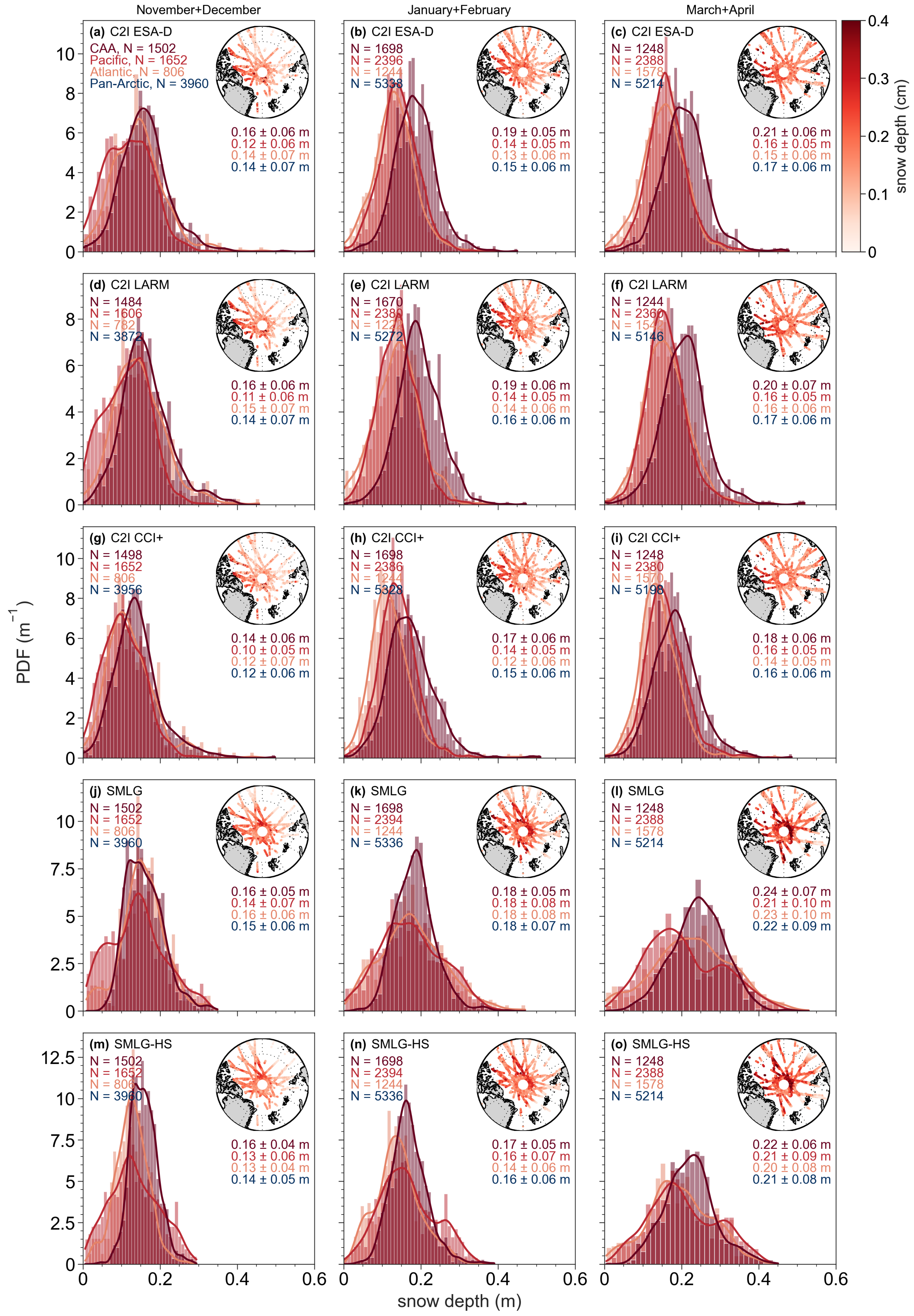

November+December
January+February
March+April
(a) C2I ESA-D
CAA, N = 1502
Pacific, N = 1652
Atlantic, N = 806
Pan-Arctic, N = 3960
0.16 ± 0.06 m
0.12 ± 0.06 m
0.14 ± 0.07 m
0.14 ± 0.07 m
(b) C2I ESA-D
N = 1698
N = 2396
N = 1244
N = 5338
0.19 ± 0.05 m
0.14 ± 0.05 m
0.13 ± 0.06 m
0.15 ± 0.06 m
(c) C2I ESA-D
N = 1248
N = 2388
N = 1578
N = 5214
0.21 ± 0.06 m
0.16 ± 0.05 m
0.15 ± 0.06 m
0.17 ± 0.06 m
snow depth (cm)
(d) C2I LARM
N = 1484
N = 1606
N = 782
N = 3872
0.16 ± 0.06 m
0.11 ± 0.06 m
0.15 ± 0.07 m
0.14 ± 0.07 m
(e) C2I LARM
N = 1670
N = 2380
N = 1222
N = 5272
0.19 ± 0.06 m
0.14 ± 0.05 m
0.14 ± 0.06 m
0.16 ± 0.06 m
(f) C2I LARM
N = 1244
N = 2360
N = 1542
N = 5146
0.20 ± 0.07 m
0.16 ± 0.05 m
0.16 ± 0.06 m
0.17 ± 0.06 m
(g) C2I CCI+
N = 1498
N = 1652
N = 806
N = 3956
0.14 ± 0.06 m
0.10 ± 0.05 m
0.12 ± 0.07 m
0.12 ± 0.06 m
(h) C2I CCI+
N = 1698
N = 2386
N = 1244
N = 5328
0.17 ± 0.06 m
0.14 ± 0.05 m
0.12 ± 0.06 m
0.15 ± 0.06 m
(i) C2I CCI+
N = 1248
N = 2380
N = 1570
N = 5198
0.18 ± 0.06 m
0.16 ± 0.05 m
0.14 ± 0.05 m
0.16 ± 0.06 m
PDF (m^-1)
(j) SMLG
N = 1502
N = 1652
N = 806
N = 3960
0.16 ± 0.05 m
0.14 ± 0.07 m
0.16 ± 0.06 m
0.15 ± 0.06 m
(k) SMLG
N = 1698
N = 2394
N = 1244
N = 5336
0.18 ± 0.05 m
0.18 ± 0.08 m
0.18 ± 0.08 m
0.18 ± 0.07 m
(l) SMLG
N = 1248
N = 2388
N = 1578
N = 5214
0.24 ± 0.07 m
0.21 ± 0.10 m
0.23 ± 0.10 m
0.22 ± 0.09 m
(m) SMLG-HS
N = 1502
N = 1652
N = 806
N = 3960
0.16 ± 0.04 m
0.13 ± 0.06 m
0.13 ± 0.04 m
0.14 ± 0.05 m
(n) SMLG-HS
N = 1698
N = 2394
N = 1244
N = 5336
0.17 ± 0.05 m
0.16 ± 0.07 m
0.14 ± 0.06 m
0.16 ± 0.06 m
(o) SMLG-HS
N = 1248
N = 2388
N = 1578
N = 5214
0.22 ± 0.06 m
0.21 ± 0.09 m
0.20 ± 0.08 m
0.21 ± 0.08 m
snow depth (m)